https://doi.org/10.5194/egusphere-2026-128
Preprint. Discussion started: 23 February 2026


# Assessment of an updated polar stratospheric cloud parameterisation for the UK Earth System Model (UKESM1.1) within the UK Met Office Unified Model (v13.9) using CALIOP and MLS observations

Isabelle Sangha[1,2], Nathan L. Abraham[3], Andrew Orr[1], Hua Lu[1], Michael C. Pitts[4], Lamont R. Poole[5], and Michael Weimer[6]

[1]British Antarctic Survey, High Cross, Madingley Road, Cambridge, CB3 0ET, UK
[2]Department of Chemistry, University of Cambridge, Cambridge, CB2 1EW, UK
[3]NCAS-Climate, University of Cambridge, CB2 1EW, UK
[4]NASA Langley Research Centre, 2 Langley Blvd, Hampton, VA 23681, USA
[5]Analytical Services & Materials, Inc., 107 Research Dr, Hampton, Virginia 23666, USA
[6]Institute of Environmental Physics, University of Bremen, Bremen, Germany

**Correspondence:** Isabelle Sangha (is568@cam.ac.uk)

**Abstract.** Accurately representing polar stratospheric clouds (PSCs) in global Chemistry-Climate Models and Earth System Models is important as they play a key role in springtime ozone depletion in polar regions by activating both chlorine and bromine species through heterogeneous reactions and denitrifying the stratosphere. Here, we present and evaluate an updated PSC parameterisation scheme implemented in the UK Earth System Model (UKESM1.1). The scheme includes the kinetic formation of nitric acid trihydrate (NAT) particles, the formation of supercooled ternary solution (STS) droplets assuming thermodynamic equilibrium, and accounts for ice and sulphate aerosols. To evaluate the new scheme, we compare modelled PSC production with satellite observations from the Cloud-Aerosol and Lidar with Orthogonal Polarization (CALIOP) instrument and model concentrations of gas-phase nitric acid and ozone concentrations with observations from the Aura Microwave Limb Sounder (MLS) instrument for the 2008 Antarctic and 2009/2010 Arctic winters. In comparison with the current, simpler scheme, the updated parameterisation increases both the range of PSC types that form and the seasonal variability, resulting in better agreement with CALIOP observations. It also slows the growth of NAT particles and enables nitric acid partitioning between gas, liquid, and solid phases, leading to improved agreement with MLS observations. However, there is comparatively little impact on stratospheric ozone, with the exception near the edge of the polar vortex where the new scheme improves comparisons with MLS observations.

## 1 Introduction

Stratospheric ozone absorbs incoming solar radiation and its depletion leads to cooling of the polar stratosphere, influencing atmospheric circulation and surface climate (Randel and Wu, 1999; Polvani et al., 2011). Polar stratospheric clouds (PSCs) play a critical role in driving ozone depletion and shaping polar stratospheric chemistry. Heterogeneous reactions on the surfaces

https://doi.org/10.5194/egusphere-2026-128
Preprint. Discussion started: 23 February 2026


of PSCs convert reservoir chlorine and bromine species into active species during the polar winter, when the absence of solar radiation allows stratospheric temperatures to drop below the thresholds for PSC formation (Solomon et al., 1986; Tritscher et al., 2021). Once sunlight returns in spring, these active species participate in catalytic cycles that efficiently destroy ozone ($O_3$), resulting in rapid $O_3$ depletion (Molina and Molina, 1987). The threshold temperature for PSC formation depends on the composition of the PSC particles. Crystalline nitric acid trihydrate (NAT) are solid particles consisting of nitric acid ($HNO_3$) and water ($H_2O$) with formation temperatures of below $T_{NAT} \sim 195$ K under normal stratospheric ambient conditions at 20 km. Supercooled ternary solution (STS) droplets form through the uptake of $HNO_3$ on the background sulphate aerosols when temperatures drop below $T_{STS} \sim 191$ K. Water ice particles form at the coldest temperatures of below $T_{ice} \sim 188$ K (Koop et al., 2000; Engel et al., 2013).

Particle composition also influences PSC surface reactivity (Carslaw et al., 1997). For many heterogeneous reactions occurring below $T_{NAT}$, liquid droplets, e.g., STS, are comparable to, or more effective than, solid NAT and ice particles in activating chlorine (Ravishankara and Hanson, 1996). Peter and Grooß (2012) showed that chlorine activation rates of NAT could only compete with the chlorine activation rates of STS in high number density 'mother clouds' that form downstream of ice clouds (Fueglistaler et al., 2002). Reaction rates on liquid binary aerosol particles also reach substantial values before NAT formation, indicating that chlorine activation is mainly driven by liquid heterogeneous chemistry. However, large solid ice and NAT particles sediment from the stratosphere into the upper troposphere, causing stratospheric denitrification and dehydration. Removal of reactive nitrogen limits the amount of nitrogen available to deactivate chlorine and prolongs periods of $O_3$ depletion (Toon et al., 1986). This effect is especially important in the Arctic, where temperatures are comparably higher and denitrification can result in greater ozone loss (Chipperfield and Pyle, 1998). In Antarctica, chlorine and bromine activation, combined with an increase in stratospheric chlorine loading due to anthropogenic release of chlorofluorocarbons, has resulted in severe springtime $O_3$ depletion in recent decades, forming a region of anomalously low total column ozone values referred to as the Antarctic ozone hole (Cicerone et al., 1974; Farman et al., 1985). This has significantly affected Southern hemisphere circulation and climate (Orr et al., 2008; Previdi and Polvani, 2014; Polvani et al., 2018).

To accurately simulate stratospheric ozone depletion, PSC parameterisation schemes in global Chemistry-Climate Models (CCMs) and Earth System Models (ESMs) must represent PSC formation and associated ozone-loss chemistry. However, the complexity of the PSC schemes in these models varies. For example, the SOCOL (SOlar Climate Ozone Links) model uses a relatively simplistic approach that assumes thermodynamic equilibrium between the PSC particles and gas phases, instantaneously forming PSCs when saturation vapour pressure is reached (Steiner et al., 2021). This requires assumptions about the particle size distribution, either number density or radius. By contrast, models such as EMAC (ECHAM5/MESSy Atmospheric chemistry model), ICON-ART (ICOsahedral Nonhydrostatic modelling framework and its Aerosol and Reactive Trace gases extension), and SD-WACCM-4.0/CARMA (Community Aerosol and Radiation Model for Atmospheres coupled to the Whole Atmosphere Community Climate Model with Specified Dynamics) use more complex methods to capture deviations from equilibrium conditions by simulating the growth and evaporation of particles, enabling a wider range of particle sizes to be represented (Kirner et al., 2011; Zhu et al., 2015; Weimer et al., 2021).

https://doi.org/10.5194/egusphere-2026-128
Preprint. Discussion started: 23 February 2026


The UK Earth System Model (UKESM1.1) uses a relatively simple approach for PSC formation, accounting only for NAT, sulphate aerosols, and ice (Dennison et al., 2019). NAT particles are nucleated assuming thermodynamic equilibrium and are assumed to have a fixed radius of 1.0 $\mu$m (Hanson and Mauersberger, 1988). Sulphate aerosols are included as a prescribed surface area density, and there is no mechanism for the formation of STS droplets (Sellar et al., 2019; Archibald et al., 2020). Ice particles are formed using the cloud microphysics scheme (Wilson and Ballard, 1999), but are assumed to have a fixed radius of 10 $\mu$m when calculating the surface area density for heterogeneous chemistry. While the exact mechanisms of NAT nucleation are still not fully understood, the growth of NAT particles occurs over hours to days (Voigt et al., 2005), and are not in equilibrium when they grow to larger sizes (Carslaw et al., 2002). Therefore, the inability of this scheme to simulate NAT outside of equilibrium conditions and to form STS particles limits the capability of UKESM1.1 to represent all PSC particle types and their evolution over the PSC season, hindering its ability to accurately simulate stratospheric ozone depletion, including projections of future ozone recovery and associated climate impacts (Austin et al., 2003; Eyring et al., 2006, 2013; Zeng et al., 2022).

PSCs are observed with satellite measurements (Pitts et al., 2013; Spang et al., 2018), ground-based lidar (Snels et al., 2019) and airborne in situ observations (Fahey et al., 2001; Voigt et al., 2003). Ground-based lidars provide measurements with high temporal resolution and enhanced signal-to-noise ratios of many variables, but their effectiveness can be limited by tropospheric cloudiness (Tesche et al., 2021). Airborne in situ measurements offer detailed observations of trace gases and aerosols, including measurements of size and number concentration, but have limited temporal and spatial coverage. Satellite-based measurements such as the Cloud-Aerosol Lidar with Orthogonal Polarization (CALIOP) onboard the Cloud-Aerosol Lidar and Infrared Pathfinder Satellite Observations (CALIPSO), which operated from June 2006 until August 2023, use the depolarization ratio to infer the particle shape and concentration, enabling distinction between liquid and solid particles (Pitts et al., 2013). Given its excellent temporal and spatial coverage and ability to differentiate PSC types, CALIOP provides a robust benchmarking dataset to evaluate PSC parameterisations. Additionally, the Microwave Limb Sounder (MLS) instrument on board the Aura Satellite flew in formation with CALIPSO in the A-Train constellation until 2018 (Stephens et al., 2002), providing nearly coincident measurements of atmospheric variables, such as $HNO_3$ and $O_3$ concentrations by observing passive thermal emissions on the millimetre and sub-millimetre wave length scale (Waters et al., 2006).

In this study, we address the limitations in the representation of NAT and STS particles in UKESM1.1 by replacing its current, simple representation of these particles with the more sophisticated representation employed in ICON-ART (Weimer et al., 2021). This approach kinetically forms NAT particles and thermodynamically forms STS particles, making it more interactive and physically based. We evaluate the performance of this new scheme relative to the current scheme by comparing modelled PSCs with CALIOP PSC observations during the 2008 Antarctic and 2009/2010 Arctic winters (Pitts et al., 2011, 2018). Comparing over both Arctic and Antarctic PSC seasons enables evaluation of the new parameterisation under the different dynamical conditions of the northern and southern polar vortices. For the Antarctic case study, we additionally investigate how the updated scheme affects the temporal evolution of PSCs and gas-phase $HNO_3$ and $O_3$ concentrations with a comparison against MLS measurements. Through these analyses, we assess how the new scheme alters UKESM1.1 PSC composition diversity and seasonal progression, while identifying remaining limitations and possible future model developments.

https://doi.org/10.5194/egusphere-2026-128
Preprint. Discussion started: 23 February 2026


## 2 Models, Data, and Methods

### 2.1 Model Descriptions

#### 2.1.1 UKESM1.1

UKESM version 1 (UKESM1.1) is a state-of-the-art Earth system model that is built around the global climate model HadGEM3-GC3.1, which is composed of the Unified Model (UM) atmosphere model, NEMO ocean model, and CICE sea ice model (Sellar et al., 2019; Mulcahy et al., 2023). Here we use version 13.9 of the UM, with a resolution of 1.875° longitude by 1.25° latitude and 85 vertical levels extending to 85 km (N96L85). Aerosols and trace gas chemistry are simulated using the stratospheric-tropospheric (Strat-Trop) configuration of the United Kingdom Chemistry and Aerosol (UKCA) model (Archibald et al., 2020), which includes v8.0 of the two-moment modal aerosol microphysics module GLOMAP-mode (Mann et al., 2010; Dhomse et al., 2014; Mulcahy et al., 2020). Strat-Trop employs 84 species and accounts for 299 reactions, including additional heterogeneous bromine reactions and updated uptake coefficients on aerosols and solid-phase PSCs implemented in UKESM1.1 (for more details, see Dennison et al., 2019).

In the original PSC parametrisation used by UKESM1.1, NAT is calculated following Chipperfield (1999), assuming thermodynamic equilibrium with gas-phase $HNO_3$ and water vapour. NAT is formed every time step when the partial pressure of $HNO_3$, $p_{HNO_3}$, exceeds the saturation vapour pressure of $HNO_3$ over NAT, $p^{NAT}_{HNO_3}$, calculated using the relationship defined in Hanson and Mauersberger (1988):

$$\log_{10}(p^{NAT}_{HNO_3}) = a_{NAT}(T) \times \log_{10}(p_{H_2O}) + b_{NAT}(T), \tag{1}$$

where $T$ is the temperature, $p_{H_2O}$ is the partial pressure of $H_2O$, and

$$a_{NAT}(T) = -2.7836 - 0.00088(T), \tag{2}$$

$$b_{NAT}(T) = 38.9855 - \frac{11397.0}{T} + 0.009179(T). \tag{3}$$

This is only valid for the temperature range $180\ \text{K} < T < 200\ \text{K}$. For temperatures below 180 K, $p^{NAT}_{HNO_3}$ is calculated with $T = 180$ K. All NAT particles are assumed to have a fixed-value radius, $r_{NAT}$, of 1.0 $\mu$m. Denitrification is prescribed based on Chipperfield (1999) with two different sedimentation velocities: one for pure NAT (0.46 mm $s^{-1}$) and one for mixed ice/NAT (17 mm $s^{-1}$) (Morgenstern et al., 2009).

Ice abundance is taken from the UM microphysics scheme which calculates the mass mixing ratio of ice using a single-moment scheme (Wilson and Ballard, 1999). The mass mixing ratio is then converted to a surface area density by assuming a radius, $r_{ice}$, of 10.0 $\mu$m. STS formation is not explicitly included; instead, the effect of liquid droplets are accounted for with a prescribed surface area density climatology from 1850 –2014 prepared for the CMIP6 model intercomparison (Sellar et al., 2019; Archibald et al., 2020) Consequently, heterogeneous reaction rates are therefore calculated based on uptake on ice, NAT, and sulphate aerosols.

https://doi.org/10.5194/egusphere-2026-128
Preprint. Discussion started: 23 February 2026


### 2.1.2 Updated PSC parameterisation

In the updated PSC scheme, the nucleation, growth, and evaporation of NAT particles is parameterised based on the analytic expression described in Carslaw et al. (2002). This is the same scheme implemented in ICON-ART, which was developed based on version 2.1 of ICON-ART (Schröter et al., 2018) and included in the published version 2025.04 (Hoshyaripour et al., 2025). Here, the time-dependent diffusive growth of the radius of a NAT particle, $r_{\mathrm{NAT}}$, is estimated by:

$$\frac{dr_{\mathrm{NAT}}}{dt} = \frac{G}{r_{\mathrm{NAT}}}, \tag{4}$$

where $t$ is time, and $G$ is the surface growth factor computed using:

$$G = \frac{D^*_{\mathrm{HNO_3}} M_{\mathrm{NAT}}}{\rho_{\mathrm{NAT}} RT}(p_{\mathrm{HNO_3}} - p^{\mathrm{NAT}}_{\mathrm{HNO_3}}), \tag{5}$$

where $M_{\mathrm{NAT}}$ is the molar mass of NAT, $\rho_{\mathrm{NAT}}$ its density, and $R$ the universal gas constant. $D^*_{\mathrm{HNO_3}}$ denotes the diffusion coefficient of $HNO_3$ in air, accounting for non-continuum mass transfer effects of particles comparable in size to the mean free path and is computed using:

$$D^*_{\mathrm{HNO_3}} = \frac{D_{\mathrm{HNO_3}}}{1 + 4D_{\mathrm{HNO_3}}/(\bar{c}_{\mathrm{HNO_3}} r_{\mathrm{NAT}})}, \tag{6}$$

where $D_{\mathrm{HNO_3}}$ is the diffusion coefficient of $HNO_3$ in air, and $\bar{c}_{\mathrm{HNO_3}}$ is the mean molecular speed of $HNO_3$.

To determine the new $r_{\mathrm{NAT}}$ at each time step as a result of growth or evaporation, Eq. (4) is integrated over time, $t$, which gives:

$$r^2_{\mathrm{NAT}}(t + \Delta t) = r^2_{\mathrm{NAT}}(t) + 2G\Delta t, \tag{7}$$

where $\Delta t$ is the chemistry time step (equal to 1 hr in UKESM1.1).

To implement the kinetic NAT formulation in UKESM1.1, size bins with fixed radii are defined according to van den Broek et al. (2004). Nine bins, each with an average radius $r_{\mathrm{NAT,b}}$ and number density limit, $n_{\mathrm{NAT,lim,b}}$, where $b$ is the bin index, span radii from 0.1 $\mu$m to 22.5 $\mu$m, based on the observed range and distribution (Fahey et al., 2001). This results in a total maximum NAT number density limit, $n_{\mathrm{NAT,max}} = \sum_b n_{\mathrm{NAT,lim,b}}$. In this study a range of values for $n_{\mathrm{NAT,max}}$ are used to assess the sensitivity to NAT number density. Regardless of the choice of value for $n_{\mathrm{NAT,max}}$, NAT initially nucleates in the smallest bin ($r_{\mathrm{NAT}}$ of 0.1 $\mu$m) with a number density of 1.5 x $10^{-5}$ $\mathrm{cm}^{-3}$ when $p_{\mathrm{HNO_3}} > p^{\mathrm{NAT}}_{\mathrm{HNO_3}}$ (see Eq. 1) with a 3 K temperature threshold included to account for homogeneous nucleation of smaller NAT particles (Peter et al., 1991). The condition thus becomes:

$$p_{\mathrm{HNO_3}} > p^{\mathrm{NAT}}_{\mathrm{HNO_3}}(T + 3\mathrm{K}) \tag{8}$$

The change in particle radius within each size bin is calculated sequentially from the smallest to the largest bin using Eq. (4) and the bin-specific growth factor $G_{\mathrm{b}}$ following Eq (5). Changes in radius are immediately converted to changes in number

https://doi.org/10.5194/egusphere-2026-128
Preprint. Discussion started: 23 February 2026


density, $n_{\mathrm{NAT,b}}$, by conserving mass, ensuring all particles in a bin have the same size. If $n_{\mathrm{NAT,b}}$ exceeds its limit $n_{\mathrm{NAT,lim,b}}$, excess mass is transferred to the next larger bin. Evaporation occurs when $p_{\mathrm{HNO_3}} < p^{\mathrm{NAT}}_{\mathrm{HNO_3}}$, making $G_{\mathrm{b}}$ negative in Eq. (5). At $T$ > 220 K, particles fully evaporate. Each size bin is treated as a separate tracer and NAT sedimentation is determined interactively, with the fall velocity calculated for each bin based on $r_{\mathrm{NAT,b}}$.

In the updated PSC scheme, STS droplets are formed by calculating the volume density of the sulphate aerosols or STS, $V_{\mathrm{STS}}$, based on the uptake of $HNO_3$ and $H_2O$ on aqueous sulphuric acid aerosols using the thermodynamic scheme documented in Carslaw et al. (1995). If $T > T_{\mathrm{STS}}$, $V_{\mathrm{STS}}$ corresponds to binary sulphate aerosols. If $T < T_{\mathrm{STS}}$, it corresponds to ternary solution droplets. $V_{\mathrm{STS}}$ is then converted to a surface area density, $S_{\mathrm{STS}}$ , for heterogeneous chemistry using the relationship described in Grainger et al. (1995):

$$S_{\mathrm{STS}} = a_{\mathrm{SV}}(V_{\mathrm{STS}})^{b_{\mathrm{SV}}}, \tag{9}$$

where $a_{\mathrm{SV}} = 6.068$ and $b_{\mathrm{SV}} = 0.671$ based on the empirical parameter fitting (Hervig and Deshler, 1998). The mean radius of the STS particles, $r_{\mathrm{STS}}$, used when calculating the optical properties, is then determined by:

$$r_{\mathrm{STS}} = \frac{3V_{\mathrm{STS}}}{S_{\mathrm{STS}}}. \tag{10}$$

To implement the new STS scheme in UKESM1.1, the concentration of aqueous sulphuric acid aerosols is provided each timestep from the interactive GLOMAP aerosol microphysical module (Mann et al., 2010; Dhomse et al., 2014; Mulcahy et al., 2020) and is used to calculate $V_{\mathrm{STS}}$. Note that the STS routine is called before the NAT routine in UKCA. This means that when temperatures fall below $T_{\mathrm{STS}}$, $HNO_3$ uptake on sulphate aerosols is calculated first. The formation, growth, or evaporation of NAT is then calculated based on the remaining gas-phase $HNO_3$.

The new PSC scheme still computes ice PSCs using the UM microphysics scheme, but the conversion from mass mixing ratio to surface area density has been modified. Previously, ice mass mixing ratio was converted to a surface area density assuming a fixed radius ($r_{\mathrm{ice}} = 10\ \mu$m). With this assumption, the ice number density, $n_{\mathrm{ice}}$, doesn't exceed 0.01 cm$^{-3}$, and the resulting surface area density remains below 2.5 $\mu$m$^2$cm$^{-3}$ for the periods analysed in this study. Although observations of ice PSC size distributions are limited, these values are relatively low compared to other PSC schemes (Zhu et al., 2017; Tritscher et al., 2019; Weimer et al., 2021). Therefore, following the approach of ICON-ART, in the updated PSC scheme the ice surface area density is instead calculated assuming a fixed value for $n_{\mathrm{ice}}$ (Weimer, 2019). However, although ICON-ART uses $n_{\mathrm{ice}}$ = 0.25 cm$^{-3}$, in this study we examine a range of $n_{\mathrm{ice}}$ values to assess the sensitivity of the results to this. For example, using higher $n_{\mathrm{ice}}$ values produce smaller ice particles with larger surface area densities.

With a prescribed $n_{\mathrm{ice}}$, stratospheric $r_{\mathrm{ice}}$ is calculated as follows:

$$r_{\mathrm{ice}} = \frac{1}{2}\sqrt[3]{\frac{m_{\mathrm{ice}}}{130}}, \tag{11}$$

where $m_{\mathrm{ice}}$ is the mass of ice particles, defined as

$$m_{\mathrm{ice}} = \frac{\rho W_{\mathrm{ice}}}{n_{\mathrm{ice}}}, \tag{12}$$

with $W_{\mathrm{ice}}$ the water mass mixing ratio of cloud ice and $\rho$ the air density (Doms et al., 2011).

https://doi.org/10.5194/egusphere-2026-128
Preprint. Discussion started: 23 February 2026


## 2.2 Observations

CALIOP was a dual-wavelength, polarization-sensitive lidar that observed profiles of the parallel and perpendicular components of the backscatter coefficients ($\beta_\perp$ and $\beta_\parallel$, respectively) at 532 nm and total backscatter at 1064 nm from mid-June 2006–August 2023 (Pitts et al., 2018). In this study, we use the CALIPSO lidar level 2 PSC mask version 2.0 (v2) which has a horizontal resolution of 5 km and vertical resolution of 180 m, and considers only nighttime measurements. This dataset was derived using the CALIOP v2 PSC Classification Algorithm (Pitts et al., 2018). For PSC detection, only the 532 nm backscatter coefficient measurements are used. The Modern-Era Retrospective analysis for Research and Applications (Gelaro et al., 2017) molecular number density is used in the theoretical calculation described in Hostetler et al. (2006) to determine the molecular backscatter, $\beta_{\text{mol}}$, which is then used to compute the 532 nm attenuated scattering ratio, $R_{532}$:

$$R_{532} = \frac{\beta_\parallel + \beta_\perp}{\beta_{\text{mol}}}. \tag{13}$$

PSCs are identified as statistical outliers in $\beta_\perp$ or $R_{532}$. Daily threshold values of $\beta_\perp$ and $R_{532}$ are defined as the median plus one median absolute deviation ($\beta_{\perp,\text{threshold}}$ and $R_{\text{threshold}}$, respectively). A PSC occurrence is then defined as exceeding either background threshold by at least the measurement uncertainty, $\sigma$:

$$\beta_\perp > \beta_{\perp,\text{threshold}} + \sigma(\beta_\perp), \tag{14}$$

$$R_{532} > R_{\text{threshold}} + \sigma(R_{532}). \tag{15}$$

where $\sigma(\beta_\perp)$ and $\sigma(R_{532})$ are computed using the noise-scale factor approach of Liu et al. (2006) as described for CALIOP by Hostetler et al. (2006). PSCs with $\beta_\perp$ exceeding the background threshold are assumed to contain non-spherical (i.e., solid) particles. $R_{532}$ is used to further classify solid-containing PSCs as either liquid-NAT mixtures (NATmix), enhanced NAT mixtures with $r_{\text{NAT}} \lesssim 3$ $\mu$m and NAT volume density $\gtrsim 1.0$ $\mu\text{m}^3\text{cm}^{-3}$ (enhNAT), ice, or high-number-density ice that forms in mountain waves (wave ice). The $R_{532}$ boundary separating enhNAT and NATmix from ice, $R_{\text{NATice}}$ is calculated dynamically from coincident cloud-free MLS gas-phase $HNO_3$ and $H_2O$ data and theoretical $R_{532}$ values for fully developed STS. PSCs below $\beta_{\perp,\text{threshold}}$, but above $R_{\text{threshold}}$ are classified as STS. Classification boundaries are summarised in Table 1, though it is important to note that they are not all-inclusive, i.e., enhNAT might not capture all NAT mixture PSCs that are heterogeneously nucleated downstream of wave ice PSCs.

The Aura MLS passively measures microwave thermal emissions from the ground to 90 km to retrieve profiles of about 20 trace gases and cloud properties. It takes measurements at wavelengths in the millimetre to sub-millimetre range from the limb of Earth's atmosphere from 82°S to 82°N every 25 s (Waters et al., 2006). In this study, model outputs are compared with MLS level 2 data (Livesey et al., 2006) for $HNO_3$ and $O_3$. The MLS $HNO_3$ product is derived from the 240-GHz retrievals at pressures $\geq$ 22 hPa and 190-GHz retrievals for lower pressures, with a vertical resolution of $HNO_3$ data is 3–4 km in the region of interest. The MLS $O_3$ product uses the 240-GHz radiances and has a vertical resolution of 2.5 km.

https://doi.org/10.5194/egusphere-2026-128
Preprint. Discussion started: 23 February 2026


**Table 1.** Boundaries in $R_{532}$ and $\beta_{\perp}$ values used to classify PSC observations using CALIOP v2 PSC classification. Threshold $\beta_{\perp,\text{threshold}}$ and $R_{\text{threshold}}$ are the median plus one median absolute deviation, and $\sigma(\beta_{\perp})$ and $\sigma(R_{532})$ are the measurement uncertainties of $\beta_{\perp}$ and $R_{532}$ respectively. The boundary between ice and both NATmix and enhNAT, $R_{\text{NATice}}$, is calculated dynamically.

| Classification | $\beta_{\perp}$ boundaries | $R_{532}$ boundaries |
|---|---|---|
| **Ice**: mixture of liquid sulphate aersols/STS and solid ice | $\beta_{\perp} > \beta_{\perp,\text{threshold}} + \sigma(\beta_{\perp})$ | $R_{532} > R_{\text{NATice}}$ |
| **Wave ice**: high number density ice particles presumably induced by mountain waves | $\beta_{\perp} > \beta_{\perp,\text{threshold}} + \sigma(\beta_{\perp})$ | $R_{532} > 50$ |
| **NATmix**: mixture of liquid sulphate aerosols/STS and solid NAT | $\beta_{\perp} > \beta_{\perp,\text{threshold}} + \sigma(\beta_{\perp})$ | $R_{532} < R_{\text{NATice}}$ |
| **enhNAT**: NAT mixtures with $r_{\text{NAT}} < 3\mu$m and NAT volume density $> 0.1\mu\text{m}^3\text{cm}^{-3}$ | $\beta_{\perp} > 2.5\times10^{-5}$ km$^{-2}$sr$^{-1}$ | $2 < R_{532} < R_{\text{NATice}}$ |
| **STS**: Super-cooled ternary solution particles | $\beta_{\perp} < \beta_{\perp,\text{threshold}} + \sigma(\beta_{\perp})$ | $R_{532} > R_{\text{threshold}} + \sigma(R_{532})$ |

## 2.3 Methodology

### 2.3.1 Comparing to observations

To compare PSCs simulated by UKESM1.1 with those observed by CALIOP, the particle size distributions from the model are used to calculate optical parameters as they would be observed by the satellite, i.e. $\beta_{\perp}$ and $\beta_{\parallel}$. The same classification algorithm used for CALIOP optical properties can then be applied to the model outputs. These optical properties are derived from the particle size distribution using Mie theory and T-matrix calculations implemented in the scattering codes within the Zurich Optical Microphysical Model (ZOMM) (Mishchenko et al., 1996; Hoyle et al., 2013; Engel et al., 2013). When applying this code to UKESM1.1 data, ice and NAT particles are represented as prolate spheroids with aspect ratios of 0.9, and a refractive index of 1.31 for ice and 1.48 for NAT (Engel et al., 2013; Tritscher et al., 2019).

To implement the Mie theory and T-matrix calculations, the ZOMM scattering code requires size-resolved number densities of STS, NAT, and ice as inputs. However, since UKESM1.1 outputs do not include the size distributions of all three PSC particle types, assumptions are necessary. Thus, to determine the size-resolved number densities, it is assumed that the total number density of PSC particles/sulphate aerosols is 10 cm$^{-3}$. The size-resolved number densities of NAT is determined inherently by the number density in each size bin for simulations using the new parameterisation. For the original parameterisation, the distribution is assumed to be monodisperse with a fixed radius of 1.0 $\mu$m. Sulphate aerosols and STS droplets are assumed

https://doi.org/10.5194/egusphere-2026-128
Preprint. Discussion started: 23 February 2026


**Table 2.** Average radius and number density limit of NAT particles in each size bin. The order of magnitude ($A$) of the number density limits for the bins depends on the sensitivity simulation. $A$ is set to $10^{-3}$, $10^{-4}$, and $10^{-5}$, resulting in the total maximum number density limit to equal $2.47\times10^{-2}$ cm$^{-3}$, $2.47\times10^{-3}$ cm$^{-3}$, or $2.47\times10^{-4}$ cm$^{-3}$, respectively.

| Bin | 1 | 2 | 3 | 4 | 5 | 6 | 7 | 8 | 9 |
|---|---|---|---|---|---|---|---|---|---|
| $r_{\mathrm{NAT,b}}$ ($\mu$m) | 0.1 | 0.6 | 1.5 | 4.0 | 7.5 | 10.5 | 14.0 | 18.0 | 22.5 |
| $n_{\mathrm{NAT,lim,b}}$ ($\times A$ cm$^{-3}$) | 3.29 | 3.29 | 3.29 | 3.29 | 3.29 | 3.29 | 1.64 | 1.64 | 1.64 |

to follow a lognormal distribution with a standard deviation of 1.6 and mean radius of $r_{\mathrm{STS}}$ estimated from Eq. (10). Ice is assumed to be a monodisperse distribution determined using either the prescribed radius or number density, depending on the parameterisation. To fully compare with CALIOP data, background $\beta_\perp$ and $R_{532}$ values were added to the simulated optical properties, and noise, $\sigma$, for both $\beta_\perp$ and $R_{532}$ is calculated using the CALIOP Noise Factor (CNF) defined in Tritscher et al. (2019):

$$\sigma(\beta_\perp) = \mathrm{CNF} \times \sqrt{\beta_\perp}, \tag{16}$$

$$\sigma(R_{532}) = |R_{532}| \times \sqrt{\frac{\sigma^2(\beta_\perp) + \sigma^2(\beta_\parallel)}{(\beta_\perp + \beta_\parallel)^2} + (0.03)^2}, \tag{17}$$

with CNF taken as 0.00102 (corresponding to a CALIOP horizontal averaging scale of 135 km, the best case for detection). The last term in Eq. (17) accounts for the 3% relative uncertainty in molecular backscatter. To estimate $\beta_\perp$ and $R_{532}$ with noise, a random value from a normal distribution with an expectation of the simulated $\beta_\perp$ or $R_{532}$ value and a standard deviation of either $\sigma(\beta_\perp)$ or $\sigma(R_{532})$, respectively, is chosen.

To compare UKESM1.1-simulated $HNO_3$ and $O_3$ concentrations with MLS satellite observations, the model outputs for $HNO_3$ (solid, liquid, and gas phase) and $O_3$ were interpolated to the same pressure levels as the MLS data. The MLS observations were then binned and averaged to match the UKESM1.1 horizontal grid, and the UKESM1.1 outputs were masked to only included grid cells where MLS data were available. In the original PSC parameterisation, solid-phase $HNO_3$ in NAT is combined with gas-phase $HNO_3$ at the end of the chemical time step for transport. Similarly, in the new scheme the liquid-phase $HNO_3$ in STS is added back to the gas phase at the end of the chemical time step. Therefore, to determine the concentration of gas-phase $HNO_3$ concentration during PSC formation and heterogeneous reaction rate calculations, the mixing ratio of $HNO_3$ in solid phase or liquid phase (for old and new scheme, respectively) was subtracted from the gas-phase $HNO_3$ output offline. Finally, an area-weighted zonal mean was calculated across three 10-degree latitude bands for both the MLS and UKESM1.1 data.

### 2.3.2 Simulations

UKESM1.1 simulations were run for January 2008–December 2011, covering the 2008 Antarctic winter and the 2009/2010 Arctic winter. For the Antarctic winter, we especially focus on the period July 10–18 2008, which represents typical winter

https://doi.org/10.5194/egusphere-2026-128
Preprint. Discussion started: 23 February 2026


**Table 3.** Parameter settings for total NAT number density limit ($cm^{-3}$) and ice number density ($cm^{-3}$) for each of the sensitivity simulations. RUN7, RUN8, RUN11, and RUN12 are selected for analysis in this study and are highlighted in bold and renamed according to whether $n_{NAT,max}$ or $n_{ice}$ is relatively high (H) or low (L) with respect to the four chosen simulations: $RUN_{<n_{NAT,max}><n_{ice}>}$.

| | $n_{ice}$ ($cm^{-3}$) | | | | |
|---|---|---|---|---|---|
| | | **0.001** | **0.01** | **0.1** | **0.25** |
| $n_{NAT,max}$ ($cm^{-3}$) | **$2.4\times10^{-4}$** | RUN1 | RUN2 | RUN3 | RUN4 |
| | **$2.4\times10^{-3}$** | RUN5 | RUN6 | **RUN7 ($RUN_{LL}$)** | **RUN8 ($RUN_{LH}$)** |
| | **$2.4\times10^{-2}$** | RUN9 | RUN10 | **RUN11 ($RUN_{HL}$)** | **RUN12 ($RUN_{HH}$)** |

stratospheric conditions with temperatures consistently below the PSC formation threshold (Pitts et al., 2018). By contrast, the Arctic 2009/2010 winter featured unusually cold stratospheric temperatures, i.e., up to 9 K below the climatological mean from early December 2009 to mid-January 2010, bringing regions below both $T_{NAT}$ and $T_{ice}$. This was followed by a major sudden stratospheric warming in late January driven by strong planetary wave-1 forcing (Dörnbrack et al., 2012), resulting in four distinct periods of CALIOP PSC optical regimes (Pitts et al., 2011).

All UKESM1.1 simulations use the Coupled Model Intercomparison Project Phase 6 (CMIP6) historical emission data spanning from 1750–2014 (Feng et al., 2020), Reynold's sea-surface temperature and sea-ice data (Reynolds et al., 2002), and are nudged to the fifth generation ECMWF atmospheric reanalysis of the global climate (ERA5-reanalysis) data (Hersbach et al., 2020). The optical comparison with CALIOP is examined for both case studies, while temporal PSC evolution and gas-phase $HNO_3$ and $O_3$ analysis focus on the Antarctic 2008 winter due to more consistent PSC formation.

Twelve simulations were performed using the updated PSC parameterisation with varying values defined for $n_{NAT,max}$ and $n_{ice}$ to conduct a sensitivity analysis assessing the effect of the prescribed parameters on PSC formation. $n_{NAT,max}$ was assigned values of either $2.4 \times 10^{-2}$, $2.4 \times 10^{-3}$, or $2.4 \times 10^{-4}$ $cm^{-3}$, which were chosen to cover the range of densities observed (Fahey et al., 2001; Biele et al., 2001) and used to constrain CALIOP observations (Pitts et al., 2011). The resulting size bins are summarized in Table 2. For ice PSCs, where observations are limited, $n_{ice}$ was set to 0.001, 0.01, 0.1, and 0.25 $cm^{-3}$, spanning ranges used in other models (Tritscher et al., 2019; Steiner et al., 2021; Weimer et al., 2021; Zhu et al., 2017), as well as the ice number densities considered by Pitts et al. (2018). A summary of the simulations is presented in Table 3. To avoid redundancy, we focus on analysing results from RUN7, RUN8, RUN11, and RUN12 as they best match the optical properties from CALIOP observations while illustrating sensitivity to $n_{NAT,max}$ and $n_{ice}$. These simulations have been renamed based on whether $n_{NAT,max}$ or $n_{ice}$ is relatively high (H) or low (L) with respect to the four selected simulations. For example, RUN8 has $n_{NAT,max}$ = $2.4\times10^{-3}$ $cm^{-3}$ which is relatively low and $n_{ice}$ = 0.25 $cm^{-3}$ which is relatively high, so it has been renamed $RUN_{LH}$. A control run (CONTROL) using the original PSC parameterisation was also performed for comparison.

https://doi.org/10.5194/egusphere-2026-128
Preprint. Discussion started: 23 February 2026


## 3 Results

### 3.1 Comparison with optical properties from CALIOP

To assess the results from the simulations under conditions with temperatures consistently below the PSC formation thresholds, Fig. 1 compares the simulated optical properties from CONTROL and the four selected sensitivity runs ($RUN_{LL}$, $RUN_{LH}$, $RUN_{HL}$, and $RUN_{HH}$) with CALIOP observations over the Antarctic from July 10–18 2008. During this period, CALIOP observations show distinct peaks in the NATmix and ice regions, with few points corresponding to the other three composition types. In contrast, CONTROL shows only some points classified as NATmix and almost none as ice, and instead shows a distinct peak in the enhNAT region. The CONTROL also has a narrower $R_{532}$ range than CALIOP, resulting in fewer PSC types represented. (Note: since CONTROL includes no STS particles, the STS optical signal likely arises from NAT and ice particles.) The sensitivity runs generally capture the observed spread of optical properties better but don't extend fully into the ice optical space, and also lack wave ice classifications. Instead, they exhibit a relative maxima in either the enhNAT or ice region, depending on the choice of $n_{ice}$. A second relative maxima occurs below $\beta_{\perp,\text{threshold}}$ and $R_{532,\text{ threshold}}$ extending into the NATmix region or STS region depending on the choice of $n_{NAT,max}$ and $n_{ice}$, respectively. Optical properties from all 12 sensitivity runs, demonstrating dependence these parameters, are shown in Fig. A1 in Appendix.

To further evaluate the new parameteristion, Fig. 2 compares simulated optical properties from CONTROL and the four selected sensitivity runs ($RUN_{LL}$, $RUN_{LH}$, $RUN_{HL}$, and $RUN_{HH}$) with CALIOP observations during the 2009/2010 Arctic winter, with the season separated into four distinct periods. Over the first period, from 15–30 Dec 2009, CALIOP is dominated by NATmix with no ice observed. Over the next two periods from 31 Dec 2009–14 Jan 2010 and 15–21 Jan 2010, CALIOP shows an increase in NATmix, as well as the occurrence of enhNAT and STS particles, and wave ice. In the final period from 22–28 Jan 2010, the vortex warmed above $T_{ice}$ and widespread PSC observations from CALIOP declined appreciably. Most remaining PSCs are NATmix with few STS and ice particles. In contrast, CONTROL shows PSCs dominated by enhNAT with a tail extending into the NATmix, exhibiting little variation throughout the season, i.e., little resemblance to CALIOP and almost no response to the changing atmospheric conditions.

Unlike CONTROL, the sensitivity runs show broadly similar variations in PSC types over the Arctic winter, though not as pronounced as CALIOP observations (Fig. 2). For example, during the first period (15–30 Dec 2009), $RUN_{HL}$ and $RUN_{HH}$ classify most PSCs as NATmix, in agreement with CALIOP. While during the second period (31 Dec 2009–14 Jan 2010), both these runs extend into the enhNAT region, again in agreement with CALIOP observations, but with few points classifying as ice. However, during the third period (15–21 Jan 2010), both these runs show a small cluster in the ice region along with an increase in points in the STS region, matching CALIOP, although none reach high enough $R_{532}$ to be classified as wave ice. During the fourth period (22–28 Jan 2010), both these runs show a decrease in NATmix, enhNAT, and STS, again similar to CALIOP. In contrast, $RUN_{LL}$ and $RUN_{LH}$ produce far fewer PSCs compared to $RUN_{HL}$ and $RUN_{HH}$ (Fig. 2). They also fail to capture the NATmix peaks, which are shown in CALIOP throughout most of the 2009/2010 season. Instead, these runs have most points occurring below $\beta_{\perp}$ and $R_{532}$ thresholds, reflecting low NAT number density and background scattering. Points

https://doi.org/10.5194/egusphere-2026-128
Preprint. Discussion started: 23 February 2026


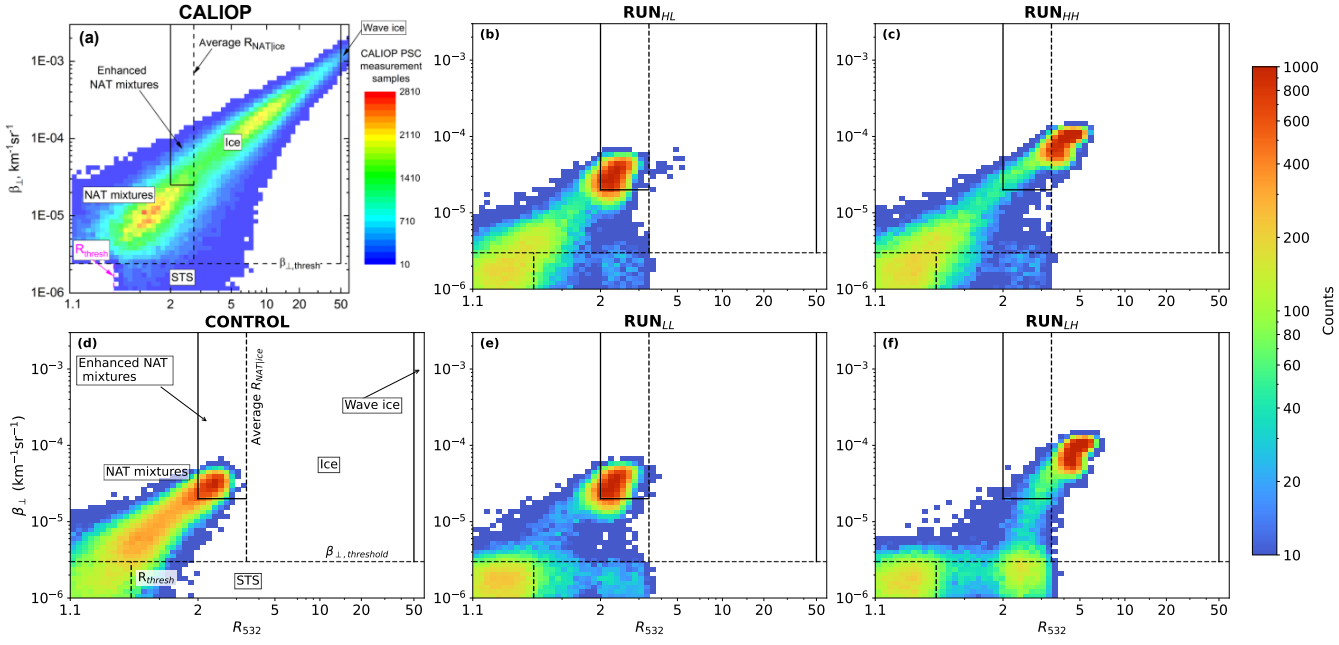


**Figure 1.** 2D histogram of optical properties from CALIOP, CONTROL, and RUN$_{LL}$, RUN$_{LH}$, RUN$_{HL}$, and RUN$_{HH}$ over the Antarctic for the period July 10–18 2008, covering a latitude range of 65°S–75°S, and potential temperature range of 475–525 K. The optical properties are plotted in the CALIOP v2 classification coordinate system of $R_{532}$ vs $\beta_\perp$. The shading indicates the number of CALIOP observations (a), or number of model grid points (b–f). Dashed lines indicate the $\beta_\perp$ an $R_{532}$ thresholds as well as the $R_{\mathrm{NATice}}$ boundary. Solid lines indicate the boundary separating wave ice, and enhanced NAT (enhNAT). The regions labelled for CONTROL (d) are the same for the sensitivity simulations (b, c, e, f).

exceeding these thresholds shift from NATmix region in the first period to STS in the second, then back to NATmix in the third period, and STS in the fourth period.

Figures 1 and 2 show that increasing $n_{\mathrm{NAT,max}}$ (i.e., comparing RUN$_{LL}$ and RUN$_{LH}$ to RUN$_{HL}$ and RUN$_{HH}$; see Table 3) shifts more points from the region below both the $\beta_\perp$ and $R_{532}$ thresholds into the regions classified as NATmix, enhNAT, and ice. In contrast, increasing $n_{\mathrm{ice}}$ (i.e., comparing RUN$_{LL}$ and RUN$_{HL}$ to RUN$_{LH}$ and RUN$_{HH}$) results in more points being classified as enhNAT or ice. The sensitivity to ice number density is more pronounced for the Antarctic case (Fig. 1), whereas sensitivity to NAT number density is more pronounced for the Arctic case (Fig. 2).

### 3.2 Temporal evolution of PSCs

To complement the optical property evaluation, Fig. 3 compares the temporal evolution of total and individual surface area densities of PSC types during the 2008 Antarctic winter season for CONTROL and RUN$_{HH}$ (which compared well with CALIOP optical properties). Note that the other selected sensitivity runs (RUN$_{LL}$, RUN$_{LH}$, and RUN$_{HL}$) showed similar results to RUN$_{HH}$ (not shown), so for brevity are not included here. The results show that CONTROL forms PSCs earlier (mid-May)

https://doi.org/10.5194/egusphere-2026-128
Preprint. Discussion started: 23 February 2026


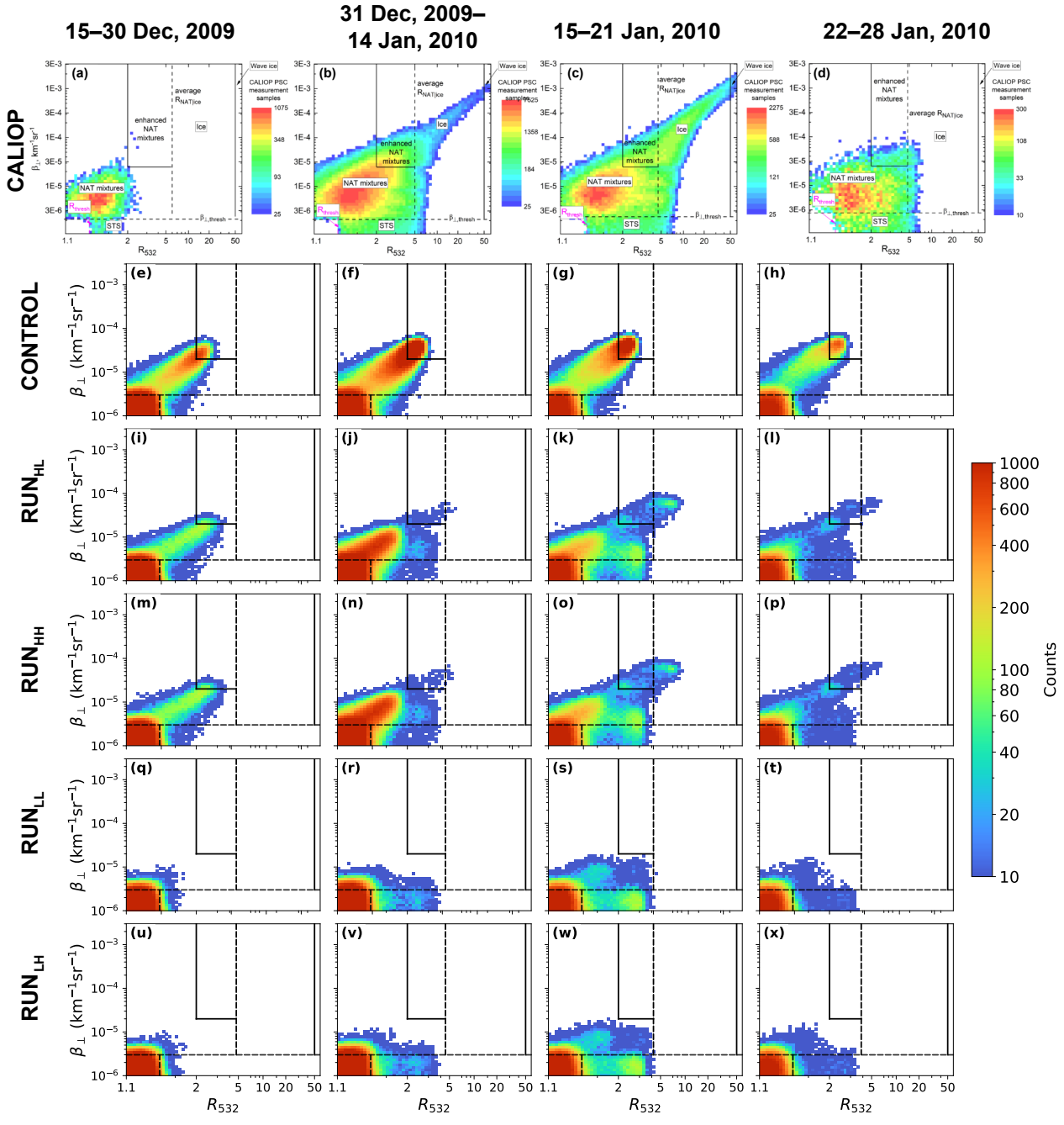


**Figure 2.** 2D histogram of optical properties from CALIOP (a–d), CONTROL (e–h), RUN$_{HL}$ (i–l), RUN$_{HH}$ (m–p), RUN$_{LL}$ (q–t), and RUN$_{LH}$ (u–x) over the Arctic for the 2009/2010 winter season, covering a latitude range of 65°N–75°N, and height range of 15–30 km. The results are separated into four distinct periods, comprising 15–30 Dec 2009 (first column), 31 Dec 2009–14 Jan 2010 (second column), 15–21 Jan 2010 (third column), and 22–28 Jan 2010 (fourth column). The results are plotted with the same classification algorithm, shading, boundaries, and regions as Fig. 1.

https://doi.org/10.5194/egusphere-2026-128
Preprint. Discussion started: 23 February 2026


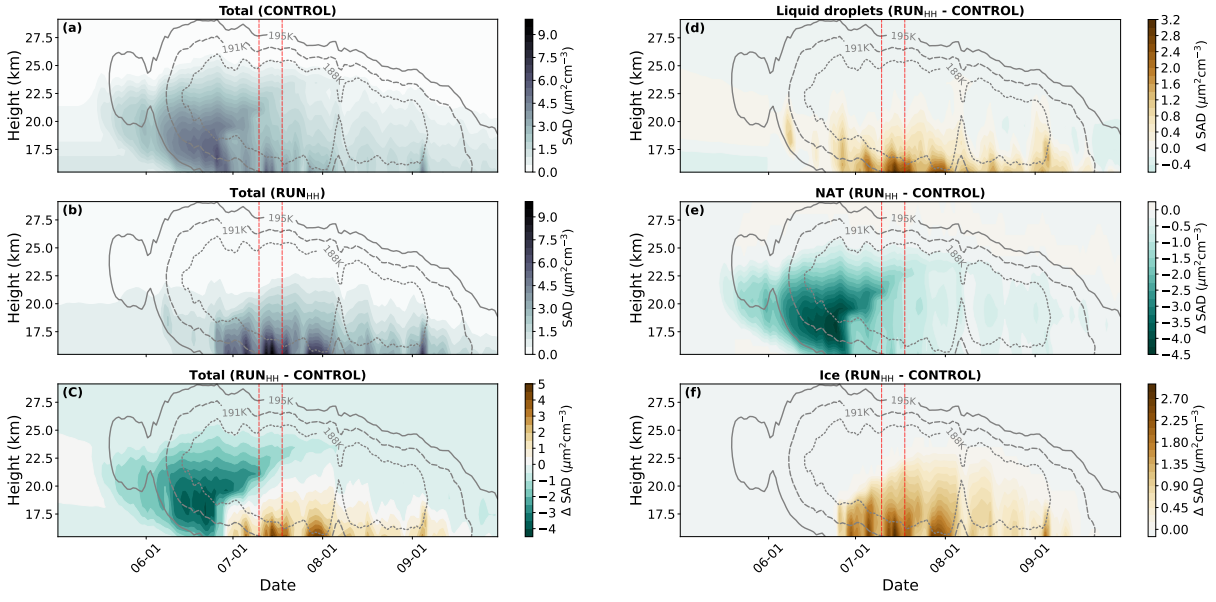


**Figure 3.** Zonal mean total surface area density (SAD) (shading; $\mu$m$^2$ cm$^{-3}$) for CONTROL (a) and RUN$_{HH}$ (b), and the difference in zonal mean SAD between RUN$_{HH}$ and CONTROL for total (c), liquid (d), NAT (e), and ice (f) PSCs over the extended 2008 Antarctic winter season (May to October), averaged across the latitude band 65°S - 90°S. Grey contour lines indicate $T_{NAT}$ (solid), $T_{STS}$ (dashed), and $T_{ice}$ (dotted). The red dashed vertical lines indicate the period July 10–18 2008 examined in Fig. 1.

than RUN$_{HH}$ (early June) and exhibits greater vertical extent, reaching 24 km compared to 22 km in RUN$_{HH}$. However, PSC formation in CONTROL declines later in the season, while RUN$_{HH}$ starts forming high surface area density PSCs which persist until early September. CONTROL therefore has larger PSC surface area densities until late-June when RUN$_{HH}$ overtakes with larger PSC surface area densities at lower altitudes through the end of the season (Fig. 3c).

Breaking these differences into the PSC types (liquid, NAT, and ice), the results show that CONTROL forms significantly more NAT early in the season, whereas RUN$_{HH}$ simulates more liquid droplets (Fig.3d) and ice particles (Fig.3f) as the season progresses. This shift from NAT dominated to STS- and ice-dominated PSCs in RUN$_{HH}$ is consistent with the PSC climatology based on CALIOP data in Pitts et al. (2018) (Fig. 16 therein), which attributes the transition to decreasing stratospheric temperatures through the austral winter. Additionally, the CALIOP climatology shows PSCs persisting into September (Antarctic spring), a feature captured by RUN$_{HH}$ but not by CONTROL.

### 3.3 Comparison of gas-phase $HNO_3$ from MLS

To further assess the simulations, Fig. 4 compares gas-phase $HNO_3$ from CONTROL and the four selected sensitivity runs (RUN$_{LL}$, RUN$_{LH}$, RUN$_{HL}$, and RUN$_{HH}$) with MLS measurements during the 2008 Antarctic winter. Over the latitude band 60°S–70°S (near the edge of the stratospheric polar vortex), MLS shows a slight drop in $HNO_3$ concentration from about 5 ppbv to 4 ppbv in July (Fig. 4a). By contrast, at 70°S–80°S (within the polar vortex), $HNO_3$ concentration drops sharply in

https://doi.org/10.5194/egusphere-2026-128
Preprint. Discussion started: 23 February 2026


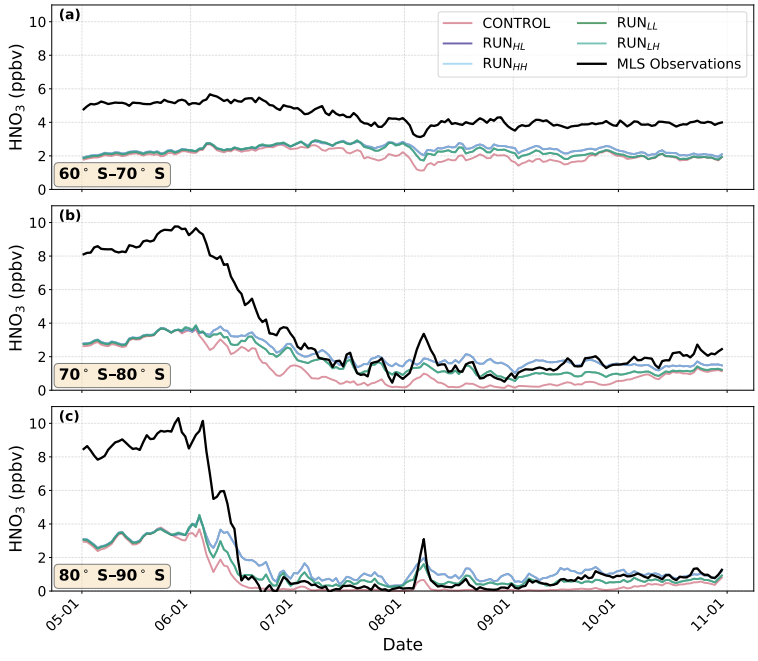


**Figure 4.** Zonal mean volume mixing ratio of gas-phase $HNO_3$ (ppbv) at 68 hPa for MLS (black line), CONTROL (pink line) and $RUN_{LL}$, $RUN_{LH}$, $RUN_{HL}$, and $RUN_{HH}$ (purple, blue, green, and teal lines, respectively) over the extended 2008 Antarctic winter season (May to October), averaged across latitude bands 60°S–70°S (a), 70°S–80°S (b), and 80°S–90°S (c). Note that there is almost complete overlap of $RUN_{HH}$ and $RUN_{HL}$, and $RUN_{LL}$ and $RUN_{LH}$, resulting in only $RUN_{HH}$ and $RUN_{LL}$ being visible in the plot.

June from 8–10 ppbv to ∼2 ppbv and remains near this level until November (Fig. 4b), reflecting removal of $HNO_3$ from the gas-phase to form PSCs. The decline is even greater at 80°S–90°S (deeper within the polar vortex), where $HNO_3$ concentration drop from 8–10 ppbv to 0 ppbv and persist until November (Fig. 4c). While both CONTROL and sensitivity runs capture the timing of depletion, they consistently underestimate $HNO_3$, especially in May before significant PSC formation. Moreover, between 70–80°S and 80–90°S, the simulated $HNO_3$ concentrations are between 3 and 4 ppbv, compared to the observed values of between 8 and 10 ppbv. This likely reflects the known bias in low total reactive nitrogen (NOy) in UKESM1.1 Strat-Trop (Archibald et al., 2020). The underestimate of $HNO_3$ concentration is most pronounced in CONTROL from mid-June to mid-October, when $HNO_3$ is being removed from the gas-phase to form PSCs. In contrast, during this same period and across the latitude bands 60°S–70°S and 70°S–80°S, the sensitivity runs show slightly higher $HNO_3$ concentrations than CONTROL, which are in closer agreement to the MLS observations. The results for $RUN_{HH}$ and $RUN_{HL}$ (both with higher $n_{NAT,max}$ values) produce the best agreement with MLS during this period of maximum depletion. A similar analysis at 100 hPa is presented in the Appendix (Fig. A3), showing consistent results with Fig. 4.

The CONTROL and the sensitivity runs treat the removal of $HNO_3$ from the gas-phase differently: CONTROL converts all removed $HNO_3$ to solid phase (NAT), whereas the sensitivity runs partition it between solid phase and liquid phase (STS).

https://doi.org/10.5194/egusphere-2026-128
Preprint. Discussion started: 23 February 2026


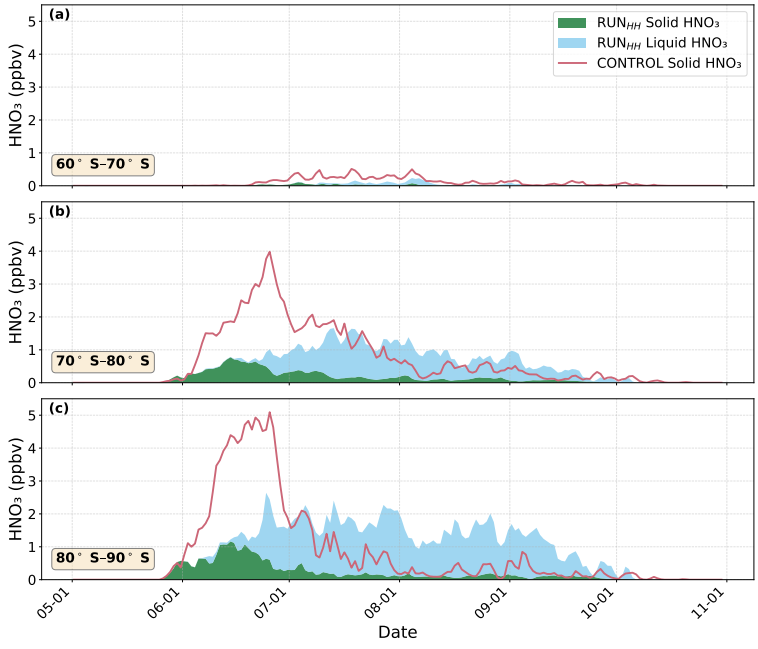


**Figure 5.** As Fig. 4, but for the zonal mean volume mixing ratio of solid-phase $HNO_3$ (ppbv) for CONTROL (pink line) and $RUN_{HH}$ (green area), as well as liquid-phase $HNO_3$ (blue area) for $RUN_{HH}$.

Figure 5 illustrates these differences for the 2008 Antarctic winter season by comparing CONTROL and $RUN_{HH}$. The results show that $RUN_{HH}$ starts partitioning $HNO_3$ from the gas phase to solid phase slightly earlier than CONTROL (early June), but once CONTROL starts forming NAT, it quickly surpasses $RUN_{HH}$ in the amount of solid-phase $HNO_3$. For example, over the latitude bands 70°S–80°S and 80°S–90°S, the amount of solid-phase $HNO_3$ simulated by CONTROL peaks in mid-June before declining in late June–early July (Fig. 5c). Conversely, $RUN_{HH}$ has a less-pronounced peak of NAT in mid-June, followed by an increase in liquid-phase $HNO_3$ as STS form. The combined solid- and liquid-phase $HNO_3$ in $RUN_{HH}$ is about half of CONTROL's mid-June peak but becomes comparable by July at 70°S–80°S and exceeds CONTROL at 80°S–90°S until October. These shifts in the amounts of solid and liquid-phase $HNO_3$ throughout the winter season are consistent with the changes in surface area density (Fig.3). A similar analysis at 100 hPa is shown in Fig. A3, which broadly agree with Fig. 5.

### 3.4 Comparison with ozone from MLS

To assess how the simulations represent ozone, Fig. 6 compares the simulated $O_3$ from CONTROL and the four selected sensitivity runs ($RUN_{LL}$, $RUN_{LH}$, $RUN_{HL}$, and $RUN_{HH}$) with MLS observations during the 2008 Antarctic winter, extending into early springtime to capture ozone depletion. The MLS data shows distinct $O_3$ loss starting around mid-August at 68 hPa, reaching near-complete depletion over latitude bands 70°S–80°S and 80°S–90°S by early October, when the Antarctic ozone hole tends to form. While both CONTROL and sensitivity runs capture the timing of $O_3$ depletion at 60°S–70°S,

https://doi.org/10.5194/egusphere-2026-128
Preprint. Discussion started: 23 February 2026


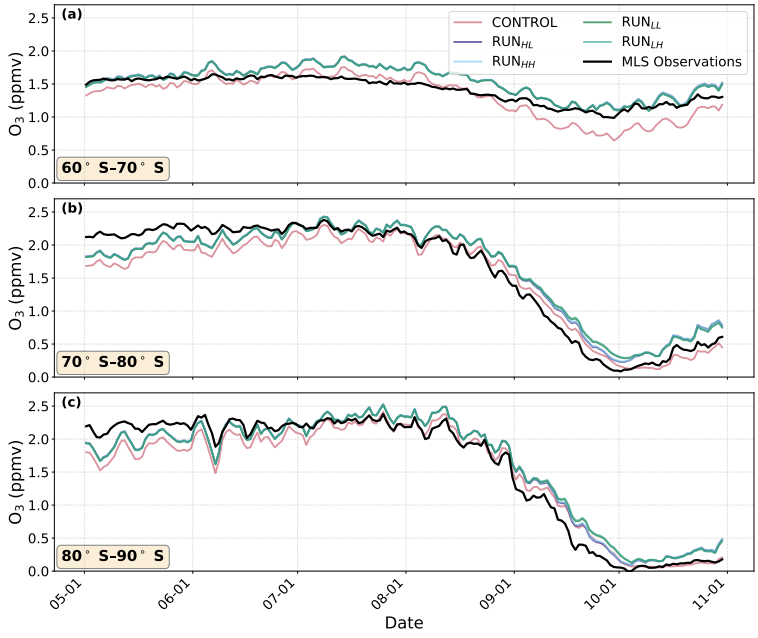


**Figure 6.** As Fig. 4, but for zonal mean $O_3$ (ppmv). Note that there is almost complete overlap of $RUN_{HH}$ and $RUN_{HL}$, and $RUN_{LL}$ and $RUN_{LH}$, resulting in only $RUN_{HH}$ and $RUN_{LL}$ being visible in the plot.

.

CONTROL underestimates $O_3$ in September–October, whereas the sensitivity runs overestimate it in June–August (Fig. 6a). At 70°S–80°S and 80°S–90°S, both CONTROL and the sensitivity runs underestimate $O_3$ in May–June, but overestimate it in August–September, with the same bias persisting into October for the sensitivity runs (Fig. 6b,c). All four sensitivity runs show comparable $O_3$ concentrations. More generally, there is often little difference between the amount of $O_3$ simulated by CONTROL and the sensitivity runs, with the exception being over the latitude band 60°S–70°S (near the edge of the polar vortex) during September–October, where the sensitivity runs agree better with MLS. At higher latitudes, improvements are marginal. A similar analysis at 100 hPa is presented in Fig. A4, with these results in general agreement with Fig. 6.

## 4 Summary

This study addresses the limitations in the representation of PSCs in UKESM1.1 by replacing its current, simple scheme with a kinetic parameterisation for NAT formation and a thermodynamic scheme for STS formation. These improvements enhance UKESM1.1's ability to represent the diversity, abundance, and seasonal evolution of PSCs. Results from a comparison of the optical properties of PSCs demonstrates that the new parameterisation achieves closer agreement with CALIOP observations during the 2008 Antarctic and 2009/2010 Arctic winters by enabling the formation of STS droplets and increasing ice surface area densities (Figs. 1 and 2). This improvement is further supported by examination of the temporal evolution of PSC surface

https://doi.org/10.5194/egusphere-2026-128
Preprint. Discussion started: 23 February 2026


area densities over the 2008 Antarctic winter, where the new parameterisation produces a greater diversity of PSC types that persist for longer (Fig. 3). Additionally, implementing a kinetic scheme for NAT formation and including the uptake of $HNO_3$ on sulphate aerosols results in gas-phase $HNO_3$ concentrations, especially at the latitude band 60°S–80°S, with improved agreement with MLS observations (Fig.4). The overall impact on stratospheric ozone is marginal during the 2008 Antarctic season (Fig. 6). However, there is a notable difference near the edge of the stratospheric polar vortex, where the sensitivity simulations show reduced ozone loss from August to October, bringing them into closer agreement with MLS observations. The lack of improvement in the representation of stratospheric ozone elsewhere may be because conditions in the centre of the vortex are already saturated: extremely cold and isolated air there allows ample PSC formation and chlorine activation. As a result, ozone loss in the polar vortex core is already maximized, so changes in PSC types have little additional impact (Kirner et al., 2015; Tritscher et al., 2021). In contrast, conditions near the vortex edge are more variable, meaning changes in PSC formation, such as slowing the growth of NAT, may have a stronger influence on heterogeneous chemistry and ozone depletion.

Furthermore, our sensitivity analysis revealed that the choice of $n_{\text{NAT,max}}$ and $n_{\text{ice}}$ directly influences the relative abundance of each PSC type (Figs. 1 and 2). Larger values of these parameters favour the formation of smaller particles with greater surface area densities. In the Arctic, the effect of $n_{\text{NAT,max}}$ is greater than $n_{ice}$, likely because the warmer stratospheric temperatures limit ice particle formation. Higher values of $n_{\text{NAT,max}}$ also improve agreement with MLS $HNO_3$ observations (Fig. 4), with $\text{RUN}_{\text{HH}}$ and $\text{RUN}_{\text{HL}}$ showing slightly lower $HNO_3$ concentrations than $\text{RUN}_{\text{LL}}$ and $\text{RUN}_{\text{LH}}$ during the period of PSC formation. This indicates that higher $n_{\text{NAT,max}}$ values result in greater $HNO_3$ uptake. However, the severe underestimation of $HNO_3$ at the beginning of the PSC season (likely due to a known low-NOy bias in the UKESM1 stratosphere discussed in Archibald et al. (2020)) means that the improved comparison with MLS $HNO_3$ data with the new parametrisation does not necessarily imply an improvement in the model's ability to accurately capture the full extent of $HNO_3$ depletion and denitrification. This is because the model begins the PSC season with less $HNO_3$ than observed. The cause of low stratospheric $HNO_3$ in UKESM1.1 requires further investigation.

In all the simulations, UKESM1.1 produced less ice than observed by CALIOP and failed to form any wave ice that was observed by CALIOP. Similar findings by Weimer et al. (2021) attribute this to the prescribed ice number density of 0.25 $\text{cm}^{-3}$, which inhibits the formation of high-number-density wave ice. Additionally, adiabatic cooling from fine-scale mountain waves propagating into the stratosphere can cause rapid, localised cooling in the stratosphere that triggers the formation of ice PSCs, which in turn can seed NAT mother clouds downstream (Drdla et al., 2002). This can result in NAT PSCs with high number densities up to 0.1–1 $\text{cm}^{-3}$ (Voigt et al., 2003) and ice PSCs with number densities up to 10 $\text{cm}^{-3}$ (Fueglistaler et al., 2003). The impact of mountain waves on total PSC formation can be substantial, even in the colder Antarctic. For example, Alexander et al. (2011) found that during the 2007 Antarctic winter, 50% of both ice and high NAT number density particles near the edge of the vortex were linked to mountain waves.

A parameterisation scheme that represents the temperature fluctuations induced by mountain waves was implemented in an earlier version of UKESM (Orr et al., 2015, 2020). Orr et al. (2020) showed that adding the parameterised cooling phase to the resolved and synoptic-scale temperatures in this model resulted in a considerable increase in the number of instances that the temperature fell below $T_{\text{NAT}}$ and $T_{\text{ice}}$ over the Antarctic Peninsula. However, as this scheme is not implemented in

https://doi.org/10.5194/egusphere-2026-128
Preprint. Discussion started: 23 February 2026


UKESM1.1, the localised rapid cooling associated with mountain waves is not represented in our simulations. Furthermore, with ice and NAT number densities prescribed in the new PSC parameterisation, there is no mechanism for high-number-density PSCs to form. To better capture cases where mountain waves trigger the formation of high-number-ddensity ice and NAT PSCs, we therefore recommend that the mountain-wave-induced temperature fluctuation scheme should be implemented into UKESM1.1. Additionally, allowing $n_{\text{ice}}$ and $n_{\text{NAT,max}}$ to depend on cooling rate would enable high-number-density ice and NAT PSC formation in regions with sudden temperature drops caused by mountain waves. Such development could further advance UKESM1.1's capability to simulate PSC formation and project future changes in polar ozone and climate (Polvani et al., 2011; Previdi and Polvani, 2014).

Nevertheless, despite the continued inability to reproduce wave ice, the updated PSC scheme presented in this study provides a more physically realistic representation of PSC formation, shows overall improvements relative to the old parameterisation, and is expected to enhance the ability of UKESM1.1 to project PSCs and stratospheric ozone.

*Code and data availability.* All simulations used in this work were performed using version 13.9 of the Met Office Unified Model coupled to the United Kingdom Chemistry and Aerosol model (UM-UKCA). The UM code branch have been made available to reviewers of this paper. Due to intellectual property copyright restrictions, the source code of the UM cannot be provided. The UKCA code used for this analysis can be accessed at DOI:10.5281/zenodo.17949939 (Sangha, 2025). The UM simulations are compiled and run in suites developed using the Rose suite engine (https://metomi.github.io/rose/doc/html/index.html, last accessed: 5 December 2025) and scheduled using the Cylc workflow engine (https://cylc.github.io/cylc/, last accessed 5 December 2025). Both Rose and Cylc are available under version 3 of the GNU General Public License (GPL). The suite contains information required to extract and build the code, and configure and run the simulations. Every suite has a unique identifier and is held in the same revision-controlled repository service as the model's code. All suites are available to any licensed user of the UM.

The ZOMM optical model code is documented in Hoyle et al. (2013) and Engel et al. (2013). CALIPSO lidar level 2 polar stratospheric cloud mask version 2.0 (v2) is available at via DOI: 10.5067/CALIOP/CALIPSO/CAL_LID_L2_PSCMASK-STANDARD-V2-00 (https://asdc.larc.nasa.gov/project/CALIPSO/CAL_LID_L2_PSCMask-Standard-V2-00_V2-00). MLS $HNO_3$ and $O_3$ data products have been downloaded from https://mls.jpl.nasa.gov/eos-aura-mls/data.php, last accessed December 5, 2025 (Manney et al., 2020; Schwartz et al., 2020).

https://doi.org/10.5194/egusphere-2026-128
Preprint. Discussion started: 23 February 2026


## Appendix A

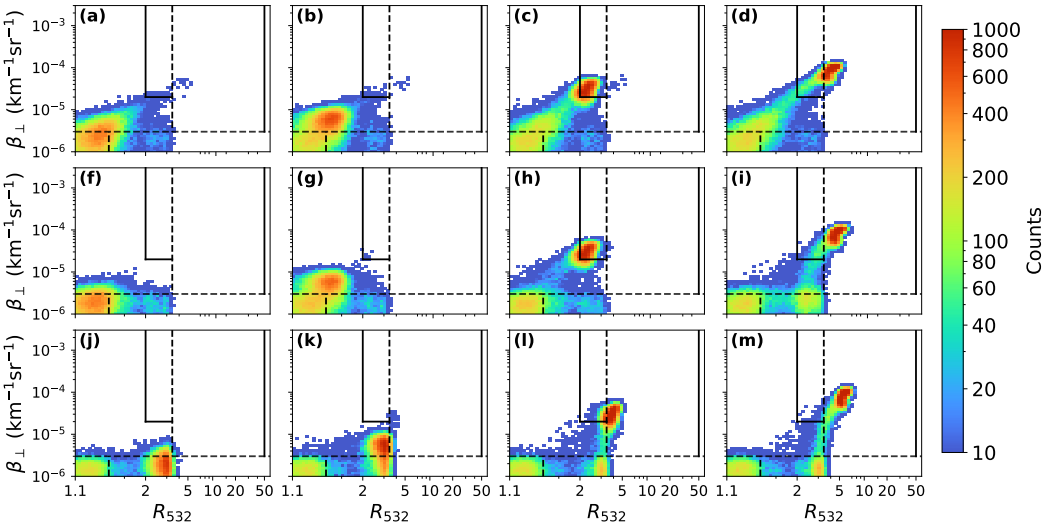


**Figure A1.** As Fig. 1 but showing the 2D histogram of optical properties from all the sensitivity simulations RUN1–RUN12 (a–m, respectively).

https://doi.org/10.5194/egusphere-2026-128
Preprint. Discussion started: 23 February 2026


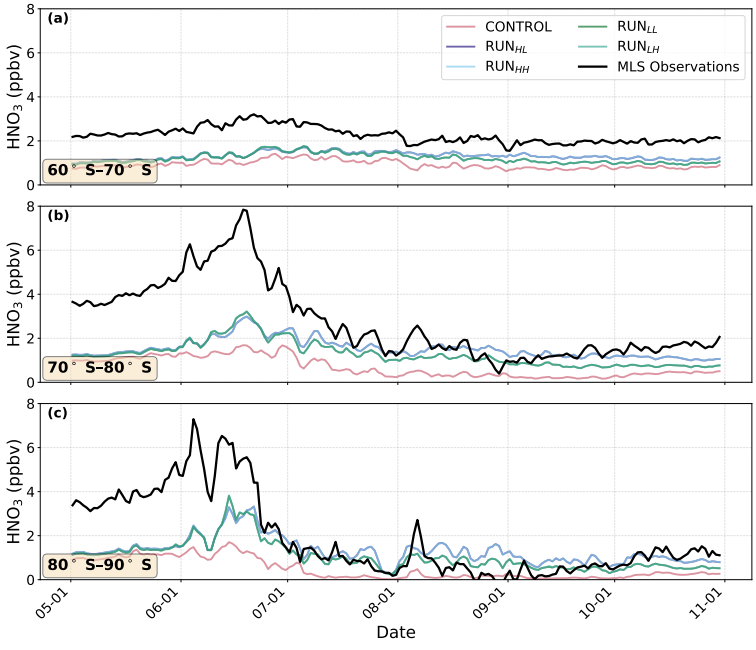


**Figure A2.** As Fig. 4, but at 100 hPa.

.

https://doi.org/10.5194/egusphere-2026-128
Preprint. Discussion started: 23 February 2026


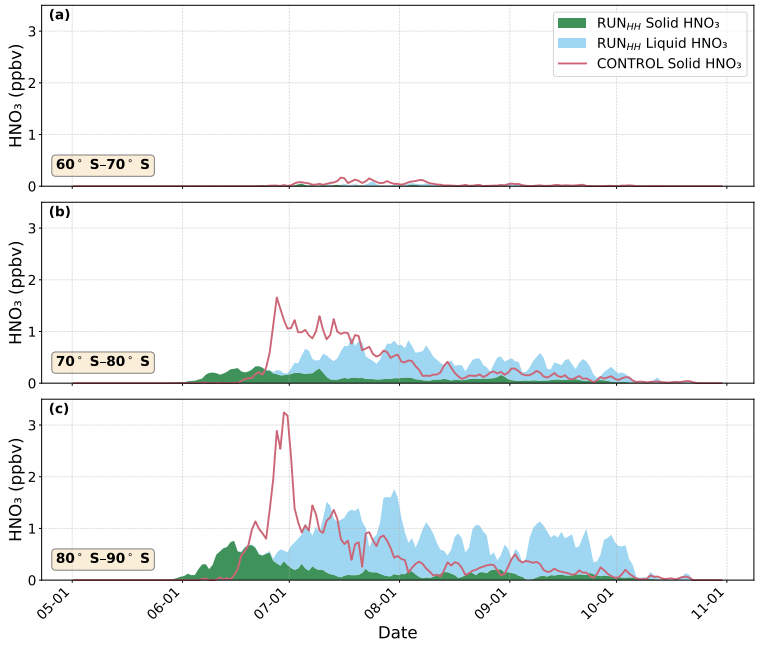


**Figure A3.** As Fig. 5, but at 100 hPa.

https://doi.org/10.5194/egusphere-2026-128
Preprint. Discussion started: 23 February 2026


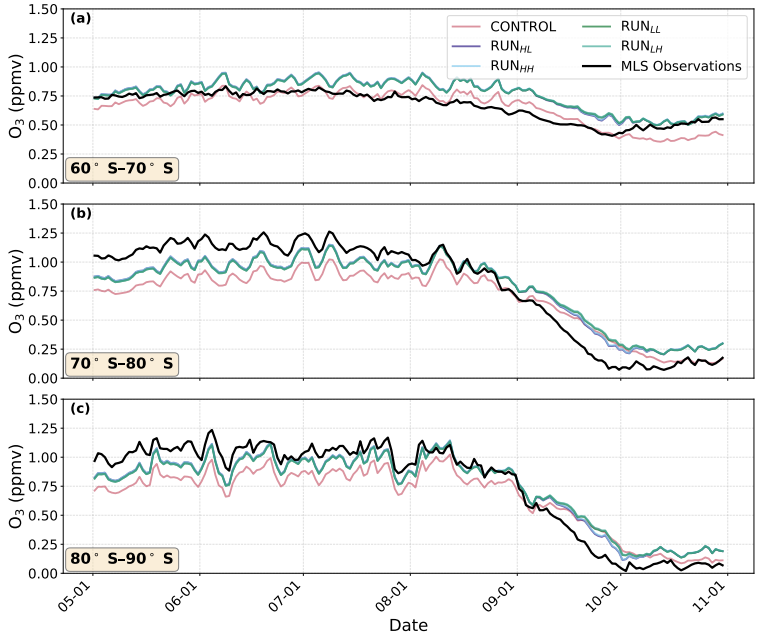


**Figure A4.** As Fig. 6, but at 100 hPa.

*Author contributions.* IS implemented the updated PSC scheme parameterisation into UKESM1.1, ran the simulations, analysed the data, and wrote the original manuscript. All authors provided guidance throughout the study and contributed to revising the manuscript. MW contributed the ICON-ART PSC code. MP and LP contributed figure panels based on CALIOP observations and ZOMM optical code.

*Competing interests.* The authors declare that they have no conflict of interests

*Acknowledgements.* IS was supported by the Natural Environment Research Council (NERC) grant number NE/S007164/1. NLA would like to thank NERC for financial support through the VISION project, NE/Z503393/1. AO was supported by NERC through the TerraFIRMA: Future Impacts, Risks and Mitigation Actions in a changing Earth System project, Grant reference NE/W004895/1. HL was supported by the NERC-CANARI project (NE/W004984/1). MP and LP were supported by funding from the project Improved characterization of PSC processes derived from a third-generation CALIOP and MLD detection and composition classification algorithm, NASA Research Opportunities in Space and Earth Sciences. This work used Monsoon3, a collaborative High-Performance Computing facility funded by the Met Office and NERC, and JASMIN, the UK collaborative data analysis facility. We thank Peter Braesicke for providing ICON-ART PSC code, Paul Field for assistance with the UKESM1.1 cloud microphysics scheme, and Alyn Lambert for support with running the ZOMM optical code.

https://doi.org/10.5194/egusphere-2026-128
Preprint. Discussion started: 23 February 2026


## References

Alexander, S. P., Klekociuk, A. R., Pitts, M. C., McDonald, A. J., and Arevalo-Torres, A.: The effect of orographic gravity waves on Antarctic polar stratospheric cloud occurrence and composition, Journal of Geophysical Research: Atmospheres, 116, https://doi.org/https://doi.org/10.1029/2010JD015184, 2011.

Archibald, A. T., O'Connor, F. M., Abraham, N. L., Archer-Nicholls, S., Chipperfield, M. P., Dalvi, M., Folberth, G. A., Dennison, F., Dhomse, S. S., Griffiths, P. T., Hardacre, C., Hewitt, A. J., Hill, R. S., Johnson, C. E., Keeble, J., Köhler, M. O., Morgenstern, O., Mulcahy, J. P., Ordóñez, C., Pope, R. J., Rumbold, S. T., Russo, M. R., Savage, N. H., Sellar, A., Stringer, M., Turnock, S. T., Wild, O., and Zeng, G.: Description and evaluation of the UKCA stratosphere–troposphere chemistry scheme (StratTrop vn 1.0) implemented in UKESM1, Geoscientific Model Development, 13, 1223–1266, https://doi.org/10.5194/gmd-13-1223-2020, 2020.

Austin, J., Shindell, D., Beagley, S. R., Brühl, C., Dameris, M., Manzini, E., Nagashima, T., Newman, P., Pawson, S., Pitari, G., Rozanov, E., Schnadt, C., and Shepherd, T. G.: Uncertainties and assessments of chemistry-climate models of the stratosphere, Atmospheric Chemistry and Physics, 3, 1–27, https://doi.org/10.5194/acp-3-1-2003, 2003.

Biele, J., Tsias, A., Luo, B. P., Carslaw, K. S., Neuber, R., Beyerle, G., and Peter, T.: Nonequilibrium coexistence of solid and liquid particles in Arctic stratospheric clouds, Journal of Geophysical Research: Atmospheres, 106, 22 991–23 007, https://doi.org/https://doi.org/10.1029/2001JD900188, 2001.

Carslaw, K. S., Luo, B., and Peter, T.: An analytic expression for the composition of aqueous HNO3-H2SO4 stratospheric aerosols including gas phase removal of HNO3, Geophysical Research Letters, 22, 1877–1880, https://doi.org/https://doi.org/10.1029/95GL01668, 1995.

Carslaw, K. S., Peter, T., and Clegg, S. L.: Modeling the composition of liquid stratospheric aerosols, Reviews of Geophysics, 35, 125–154, https://doi.org/https://doi.org/10.1029/97RG00078, 1997.

Carslaw, K. S., Kettleborough, J. A., Northway, M. J., Davies, S., Gao, R.-S., Fahey, D. W., Baumgardner, D. G., Chipperfield, M. P., and Kleinböhl, A.: A vortex-scale simulation of the growth and sedimentation of large nitric acid hydrate particles, Journal of Geophysical Research: Atmospheres, 107, 43–1, https://doi.org/https://doi.org/10.1029/2001JD000467, 2002.

Chipperfield, M. P.: Multiannual simulations with a three-dimensional chemical transport model, Journal of Geophysical Research: Atmospheres, 104, 1781–1805, https://doi.org/https://doi.org/10.1029/98JD02597, 1999.

Chipperfield, M. P. and Pyle, J. A.: Model sensitivity studies of Arctic ozone depletion, Journal of Geophysical Research: Atmospheres, 103, 28 389–28 403, https://doi.org/https://doi.org/10.1029/98JD01960, 1998.

Cicerone, R. J., Stolarski, R. S., and Walters, S.: Stratospheric Ozone Destruction by Man-Made Chlorofluoromethanes, Science, 185, 1165–1167, https://doi.org/10.1126/science.185.4157.1165, 1974.

Dennison, F., Keeble, J., Morgenstern, O., Zeng, G., Abraham, N. L., and Yang, X.: Improvements to stratospheric chemistry scheme in the UM-UKCA (v10.7) model: solar cycle and heterogeneous reactions, Geoscientific Model Development, 12, 1227–1239, https://doi.org/10.5194/gmd-12-1227-2019, 2019.

Dhomse, S. S., Emmerson, K. M., Mann, G. W., Bellouin, N., Carslaw, K. S., Chipperfield, M. P., Hommel, R., Abraham, N. L., Telford, P., and Braesicke, P.: Aerosol microphysics simulations of the Mt.˜ Pinatubo eruption with the UM-UKCA composition-climate model, Atmospheric Chemistry and Physics, 14, 11 221–11 246, 2014.

Doms, G., Förstner, J., Heise, E., Herzog, H. J., Mironov, D., Raschendorfer, M., Reinhardt, T., Ritter, B., Schrodin, R., and Schulz, J.-P.: A description of the nonhydrostatic regional COSMO model. Part II: Physical parameterization, Deutscher Wetterdienst, Offenbach, Germany, 2011.

https://doi.org/10.5194/egusphere-2026-128
Preprint. Discussion started: 23 February 2026


Dörnbrack, A., Pitts, M. C., Poole, L. R., Orsolini, Y. J., Nishii, K., and Nakamura, H.: The 2009–2010 Arctic stratospheric winter – general evolution, mountain waves and predictability of an operational weather forecast model, Atmospheric Chemistry and Physics, 12, 3659–3675, https://doi.org/10.5194/acp-12-3659-2012, 2012.

Drdla, K., Gandrud, B. W., Baumgardner, D., Wilson, J. C., Bui, T. P., Hurst, D., Schauffler, S. M., Jost, H., Greenblatt, J. B., and Webster, C. R.: Evidence for the widespread presence of liquid-phase particles during the 1999–2000 Arctic winter, Journal of Geophysical Research: Atmospheres, 107, 61–1, https://doi.org/https://doi.org/10.1029/2001JD001127, 2002.

Engel, I., Luo, B. P., Pitts, M. C., Poole, L. R., Hoyle, C. R., Grooß, J.-U., Dörnbrack, A., and Peter, T.: Heterogeneous formation of polar stratospheric clouds – Part 2: Nucleation of ice on synoptic scales, Atmospheric Chemistry and Physics, 13, 10 769–10 785, https://doi.org/10.5194/acp-13-10769-2013, 2013.

Eyring, V., Butchart, N., Waugh, D. W., Akiyoshi, H., Austin, J., Bekki, S., Bodeker, G. E., Boville, B. A., Brühl, C., Chipperfield, M. P., Cordero, E., Dameris, M., Deushi, M., Fioletov, V. E., Frith, S. M., Garcia, R. R., Gettelman, A., Giorgetta, M. A., Grewe, V., Jourdain, L., Kinnison, D. E., Mancini, E., Manzini, E., Marchand, M., Marsh, D. R., Nagashima, T., Newman, P. A., Nielsen, J. E., Pawson, S., Pitari, G., Plummer, D. A., Rozanov, E., Schraner, M., Shepherd, T. G., Shibata, K., Stolarski, R. S., Struthers, H., Tian, W., and Yoshiki, M.: Assessment of temperature, trace species, and ozone in chemistry-climate model simulations of the recent past, Journal of Geophysical Research: Atmospheres, 111, https://doi.org/https://doi.org/10.1029/2006JD007327, 2006.

Eyring, V., Arblaster, J. M., Cionni, I., Sedláček, J., Perlwitz, J., Young, P. J., Bekki, S., Bergmann, D., Cameron-Smith, P., Collins, W. J., Faluvegi, G., Gottschaldt, K.-D., Horowitz, L. W., Kinnison, D. E., Lamarque, J.-F., Marsh, D. R., Saint-Martin, D., Shindell, D. T., Sudo, K., Szopa, S., and Watanabe, S.: Long-term ozone changes and associated climate impacts in CMIP5 simulations, Journal of Geophysical Research: Atmospheres, 118, 5029–5060, https://doi.org/https://doi.org/10.1002/jgrd.50316, 2013.

Fahey, D. W., Gao, R. S., Carslaw, K. S., Kettleborough, J., Popp, P. J., Northway, M. J., Holecek, J. C., Ciciora, S. C., McLaughlin, R. J., Thompson, T. L., Winkler, R. H., Baumgardner, D. G., Gandrud, B., Wennberg, P. O., Dhaniyala, S., McKinney, K., Peter, T., Salawitch, R. J., Bui, T. P., Elkins, J. W., Webster, C. R., Atlas, E. L., Jost, H., Wilson, J. C., Herman, R. L., Kleinböhl, A., and von König, M.: The Detection of Large HNO3-Containing Particles in the Winter Arctic Stratosphere, Science, 291, 1026–1031, https://doi.org/10.1126/science.1057265, 2001.

Farman, J. C., Gardiner, B. G., and Shanklin, J. D.: Large losses of total ozone in Antarctica reveal seasonal ClOx/NOx interaction, Nature, 315, 207–210, https://doi.org/10.1038/315207a0, 1985.

Feng, L., Smith, S. J., Braun, C., Crippa, M., Gidden, M. J., Hoesly, R., Klimont, Z., van Marle, M., van den Berg, M., and van der Werf, G. R.: The generation of gridded emissions data for CMIP6, Geoscientific Model Development, 13, 461–482, https://doi.org/10.5194/gmd-13-461-2020, 2020.

Fueglistaler, S., Luo, B. P., Voigt, C., Carslaw, K. S., and Peter, T.: NAT-rock formation by mother clouds: a microphysical model study, Atmospheric Chemistry and Physics, 2, 93–98, https://doi.org/10.5194/acp-2-93-2002, 2002.

Fueglistaler, S., Buss, S., Luo, B. P., Wernli, H., Flentje, H., Hostetler, C. A., Poole, L. R., Carslaw, K. S., and Peter, T.: Detailed modeling of mountain wave PSCs, Atmospheric Chemistry and Physics, 3, 697–712, https://doi.org/10.5194/acp-3-697-2003, 2003.

Gelaro, R., McCarty, W., Suárez, M. J., Todling, R., Molod, A., Takacs, L., Randles, C. A., Darmenov, A., Bosilovich, M. G., Reichle, R., Wargan, K., Coy, L., Cullather, R., Draper, C., Akella, S., Buchard, V., Conaty, A., da Silva, A. M., Gu, W., Kim, G.-K., Koster, R., Lucchesi, R., Merkova, D., Nielsen, J. E., Partyka, G., Pawson, S., Putman, W., Rienecker, M., Schubert, S. D., Sienkiewicz, M., and Zhao, B.: The Modern-Era Retrospective Analysis for Research and Applications, Version 2 (MERRA-2), Journal of Climate, 30, 5419–5454, https://doi.org/https://doi.org/10.1175/JCLI-D-16-0758.1, 2017.

https://doi.org/10.5194/egusphere-2026-128
Preprint. Discussion started: 23 February 2026


Grainger, R. G., Lambert, A., Rodgers, C. D., Taylor, F. W., and Deshler, T.: Stratospheric aerosol effective radius, surface area and volume estimated from infrared measurements, Journal of Geophysical Research: Atmospheres, 100, 16 507–16 518, https://doi.org/https://doi.org/10.1029/95JD00988, 1995.

Hanson, D. R. and Mauersberger, K.: Laboratory studies of the nitric acid trihydrate: Implications for the south polar stratosphere, Geophysical Research Letters, 15, 855–858, https://api.semanticscholar.org/CorpusID:129932383, 1988.

Hersbach, H., Bell, B., Berrisford, P., Hirahara, S., Horányi, A., Muñoz-Sabater, J., Nicolas, J., Peubey, C., Radu, R., Schepers, D., Simmons, A., Soci, C., Abdalla, S., Abellan, X., Balsamo, G., Bechtold, P., Biavati, G., Bidlot, J., Bonavita, M., De Chiara, G., Dahlgren, P., Dee, D., Diamantakis, M., Dragani, R., Flemming, J., Forbes, R., Fuentes, M., Geer, A., Haimberger, L., Healy, S., Hogan, R. J., Hólm, E., Janisková, M., Keeley, S., Laloyaux, P., Lopez, P., Lupu, C., Radnoti, G., de Rosnay, P., Rozum, I., Vamborg, F., Villaume, S., and Thépaut, J.-N.: The ERA5 global reanalysis, Quarterly Journal of the Royal Meteorological Society, 146, 1999–2049, https://doi.org/https://doi.org/10.1002/qj.3803, 2020.

Hervig, M. E. and Deshler, T.: Stratospheric aerosol surface area and volume inferred from HALOE, CLAES, and ILAS measurements, Journal of Geophysical Research: Atmospheres, 103, 25 345–25 352, https://doi.org/https://doi.org/10.1029/98JD01962, 1998.

Hoshyaripour, G. A., Baer, A., Bierbauer, S., Bruckert, J., Brunner, D., Foerstner, J., Hamzehloo, A., Hanft, V., Keller, C., Klose, M., Kumar, P., Ludwig, P., Metzner, E., Muth, L., Pauling, A., Porz, N., Reddmann, T., Reißig, L., Ruhnke, R., Satitkovitchai, K., Seifert, A., Sinnhuber, M., Steiner, M., Versick, S., Vogel, H., Weimer, M., Werchner, S., and Hoose, C.: The Atmospheric Composition Component of the ICON modeling framework: ICON-ART version 2025.04, EGUsphere, 2025, 1–54, https://doi.org/10.5194/egusphere-2025-3400, 2025.

Hostetler, C. A., Liu, Z., Reagan, J., Vaughan, M., Winker, D., Osborn, M., Hunt, W. H., Powell, K. A., and Trepte, C.: Cloud-Aerosol Lidar with Orthogonal Polarization (CALIOP) Algorithm Theoretical Basis Document, 2006.

Hoyle, C. R., Engel, I., Luo, B. P., Pitts, M. C., Poole, L. R., Grooß, J.-U., and Peter, T.: Heterogeneous formation of polar stratospheric clouds – Part 1: Nucleation of nitric acid trihydrate (NAT), Atmospheric Chemistry and Physics, 13, 9577–9595, https://doi.org/10.5194/acp-13-9577-2013, 2013.

Kirner, O., Ruhnke, R., Buchholz-Dietsch, J., Jöckel, P., Brühl, C., and Steil, B.: Simulation of polar stratospheric clouds in the chemistry-climate-model EMAC via the submodel PSC, Geoscientific Model Development, 4, 169–182, https://doi.org/10.5194/gmd-4-169-2011, 2011.

Kirner, O., Müller, R., Ruhnke, R., and Fischer, H.: Contribution of liquid, NAT and ice particles to chlorine activation and ozone depletion in Antarctic winter and spring, Atmospheric Chemistry and Physics, 15, 2019–2030, https://doi.org/10.5194/acp-15-2019-2015, 2015.

Koop, T., Luo, B., Tsias, A., and Peter, T.: Water activity as the determinant for homogeneous ice nucleation in aqueous solutions, Nature, 406, 611–614, https://doi.org/10.1038/35020537, 2000.

Liu, Z., Hunt, W., Vaughan, M., Hostetler, C., McGill, M., Powell, K., Winker, D., and Hu, Y.: Estimating random errors due to shot noise in backscatter lidar observations, Appl. Opt., 45, 4437–4447, https://doi.org/10.1364/AO.45.004437, 2006.

Livesey, N. J., Van Snyder, W., Read, W. G., and Wagner, P. A.: Retrieval algorithms for the EOS Microwave limb sounder (MLS), IEEE Transactions on Geoscience and Remote Sensing, 44, 1144–1155, 2006.

Mann, G. W., Carslaw, K. S., Spracklen, D. V., Ridley, D. A., Manktelow, P. T., Chipperfield, M. P., Pickering, S. J., and Johnson, C. E.: Description and evaluation of GLOMAP-mode: a modal global aerosol microphysics model for the UKCA composition-climate model, Geoscientific Model Development, 3, 519–551, https://doi.org/10.5194/gmd-3-519-2010, 2010.

https://doi.org/10.5194/egusphere-2026-128
Preprint. Discussion started: 23 February 2026


Manney, G., Santee, M., Froidevaux, L., Livesey, N., and Read, W.: MLS/Aura Level 2 Nitric Acid (HNO3) Mixing Ratio V005, https://doi.org/10.5067/Aura/MLS/DATA2511, 2020.

Mishchenko, M. I., Travis, L. D., and Mackowski, D. W.: T-matrix computations of light scattering by nonspherical particles: A review, Journal of Quantitative Spectroscopy and Radiative Transfer, 55, 535–575, https://doi.org/https://doi.org/10.1016/0022-4073(96)00002-7, 1996.

Molina, L. T. and Molina, M. J.: Production of chlorine oxide (Cl2O2) from the self-reaction of the chlorine oxide (ClO) radical, Journal of Physical Chemistry, 91, 433–436, 1987.

Morgenstern, O., Braesicke, P., O'Connor, F. M., Bushell, A. C., Johnson, C. E., Osprey, S. M., and Pyle, J. A.: Evaluation of the new UKCA climate-composition model – Part 1: The stratosphere, Geoscientific Model Development, 2, 43–57, https://doi.org/10.5194/gmd-2-43-2009, 2009.

Mulcahy, J. P., Johnson, C., Jones, C. G., Povey, A. C., Scott, C. E., Sellar, A., Turnock, S. T., Woodhouse, M. T., Abraham, N. L., Andrews, M. B., Bellouin, N., Browse, J., Carslaw, K. S., Dalvi, M., Folberth, G. A., Glover, M., Grosvenor, D. P., Hardacre, C., Hill, R., Johnson, B., Jones, A., Kipling, Z., Mann, G., Mollard, J., O'Connor, F. M., Palmiéri, J., Reddington, C., Rumbold, S. T., Richardson, M., Schutgens, N. A. J., Stier, P., Stringer, M., Tang, Y., Walton, J., Woodward, S., and Yool, A.: Description and evaluation of aerosol in UKESM1 and HadGEM3-GC3.1 CMIP6 historical simulations, Geoscientific Model Development, 13, 6383–6423, https://doi.org/10.5194/gmd-13-6383-2020, 2020.

Mulcahy, J. P., Jones, C. G., Rumbold, S. T., Kuhlbrodt, T., Dittus, A. J., Blockley, E. W., Yool, A., Walton, J., Hardacre, C., Andrews, T., Bodas-Salcedo, A., Stringer, M., de Mora, L., Harris, P., Hill, R., Kelley, D., Robertson, E., and Tang, Y.: UKESM1.1: development and evaluation of an updated configuration of the UK Earth System Model, Geoscientific Model Development, 16, 1569–1600, https://doi.org/10.5194/gmd-16-1569-2023, 2023.

Orr, A., Marshall, G. J., Hunt, J. C. R., Sommeria, J., Wang, C.-G., van Lipzig, N. P. M., Cresswell, D., and King, J. C.: Characteristics of Summer Airflow over the Antarctic Peninsula in Response to Recent Strengthening of Westerly Circumpolar Winds, Journal of the Atmospheric Sciences, 65, 1396–1413, https://doi.org/https://doi.org/10.1175/2007JAS2498.1, 2008.

Orr, A., Hosking, J. S., Hoffmann, L., Keeble, J., Dean, S. M., Roscoe, H. K., Abraham, N. L., Vosper, S., and Braesicke, P.: Inclusion of mountain-wave-induced cooling for the formation of PSCs over the Antarctic Peninsula in a chemistry–climate model, Atmospheric Chemistry and Physics, 15, 1071–1086, https://doi.org/10.5194/acp-15-1071-2015, 2015.

Orr, A., Scott Hosking, J., Delon, A., Hoffmann, L., Spang, R., Moffat-Griffin, T., Keeble, J., Luke Abraham, N., Braesicke, P., and Orr, A.: Polar stratospheric clouds initiated by mountain waves in a global chemistry-climate model: A missing piece in fully modelling polar stratospheric ozone depletion, Atmospheric Chemistry and Physics, 20, https://doi.org/10.5194/acp-20-12483-2020, 2020.

Peter, T. and Grooß, J.-U.: Polar stratospheric clouds and sulfate aerosol particles: microphysics, denitrification and heterogeneous chemistry, Stratospheric ozone depletion and climate change, pp. 108–144, 2012.

Peter, T., Brühl, C., and Crutzen, P. J.: Increase in the PSC-formation probability caused by high-flying aircraft, Geophysical Research Letters, 18, 1465–1468, https://doi.org/https://doi.org/10.1029/91GL01562, 1991.

Pitts, M. C., Poole, L. R., Dörnbrack, A., and Thomason, L. W.: The 2009–2010 Arctic polar stratospheric cloud season: a CALIPSO perspective, Atmospheric Chemistry and Physics, 11, 2161–2177, https://doi.org/10.5194/acp-11-2161-2011, 2011.

Pitts, M. C., Poole, L. R., Lambert, A., and Thomason, L. W.: An assessment of CALIOP polar stratospheric cloud composition classification, Atmospheric Chemistry and Physics, 13, 2975–2988, https://doi.org/10.5194/acp-13-2975-2013, 2013.

https://doi.org/10.5194/egusphere-2026-128
Preprint. Discussion started: 23 February 2026


Pitts, M. C., Poole, L. R., and Gonzalez, R.: Polar stratospheric cloud climatology based on CALIPSO spaceborne lidar measurements from 2006 to 2017, Atmospheric Chemistry and Physics, 18, 10 881–10 913, https://doi.org/10.5194/acp-18-10881-2018, 2018.

Polvani, L., Waugh, D., Correa, G., and Son, S.-W.: Stratospheric Ozone Depletion: The Main Driver of Twentieth-Century Atmospheric Circulation Changes in the Southern Hemisphere, Journal of Climate - J CLIMATE, 24, 795–812, https://doi.org/10.1175/2010JCLI3772.1, 2011.

Polvani, L. M., Abalos, M., Garcia, R., Kinnison, D., and Randel, W. J.: Significant Weakening of Brewer-Dobson Circulation Trends Over the 21st Century as a Consequence of the Montreal Protocol, Geophysical Research Letters, 45, 401–409, https://doi.org/https://doi.org/10.1002/2017GL075345, 2018.

Previdi, M. and Polvani, L. M.: Climate system response to stratospheric ozone depletion and recovery, Quarterly Journal of the Royal Meteorological Society, 140, 2401–2419, https://doi.org/https://doi.org/10.1002/qj.2330, 2014.

Randel, W. J. and Wu, F.: Cooling of the Arctic and Antarctic Polar Stratospheres due to Ozone Depletion, Journal of Climate, 12, 1467–1479, https://doi.org/https://doi.org/10.1175/1520-0442(1999)012<1467:COTAAA>2.0.CO;2, 1999.

Ravishankara, A. R. and Hanson, D. R.: Differences in the reactivity of type I polar stratospheric clouds depending on their phase, Journal of Geophysical Research: Atmospheres, 101, 3885–3890, https://doi.org/https://doi.org/10.1029/95JD03009, 1996.

Reynolds, R. W., Rayner, N. A., Smith, T. M., Stokes, D. C., and Wang, W.: An Improved In Situ and Satellite SST Analysis for Climate, Journal of Climate, 15, 1609–1625, https://doi.org/https://doi.org/10.1175/1520-0442(2002)015<1609:AIISAS>2.0.CO;2, 2002.

Sangha, I.: UKCA PSC branch, https://doi.org/DOI:10.5281/zenodo.17949939, 2025.

Schröter, J., Rieger, D., Stassen, C., Vogel, H., Weimer, M., Werchner, S., Förstner, J., Prill, F., Reinert, D., and Zängl, G.: ICON-ART 2.1: A flexible tracer framework and its application for composition studies in numerical weather forecasting and climate simulations, Geoscientific Model Development, 11, 4043–4068, 2018.

Schwartz, M., Froidevaux, L., Livesey, N., and Read, W.: MLS/Aura Level 2 Ozone (O3) Mixing Ratio V005, https://doi.org/10.5067/Aura/MLS/DATA2516, 2020.

Sellar, A. A., Jones, C. G., Mulcahy, J. P., Tang, Y., Yool, A., Wiltshire, A., O'Connor, F. M., Stringer, M., Hill, R., Palmieri, J., Woodward, S., de Mora, L., Kuhlbrodt, T., Rumbold, S. T., Kelley, D. I., Ellis, R., Johnson, C. E., Walton, J., Abraham, N. L., Andrews, M. B., Andrews, T., Archibald, A. T., Berthou, S., Burke, E., Blockley, E., Carslaw, K., Dalvi, M., Edwards, J., Folberth, G. A., Gedney, N., Griffiths, P. T., Harper, A. B., Hendry, M. A., Hewitt, A. J., Johnson, B., Jones, A., Jones, C. D., Keeble, J., Liddicoat, S., Morgenstern, O., Parker, R. J., Predoi, V., Robertson, E., Siahaan, A., Smith, R. S., Swaminathan, R., Woodhouse, M. T., Zeng, G., and Zerroukat, M.: UKESM1: Description and Evaluation of the U.K. Earth System Model, Journal of Advances in Modeling Earth Systems, 11, 4513–4558, https://doi.org/https://doi.org/10.1029/2019MS001739, 2019.

Snels, M., Scoccione, A., Di Liberto, L., Colao, F., Pitts, M., Poole, L., Deshler, T., Cairo, F., Cagnazzo, C., and Fierli, F.: Comparison of Antarctic polar stratospheric cloud observations by ground-based and space-borne lidar and relevance for chemistry–climate models, Atmospheric Chemistry and Physics, 19, 955–972, https://doi.org/10.5194/acp-19-955-2019, 2019.

Solomon, S., Garcia, R., Rowland, F., and Wuebbles, D.: On the Depletion of Antarctic Ozone, Nature, 321, 755–758, https://doi.org/10.1038/321755a0, 1986.

Spang, R., Hoffmann, L., Müller, R., Grooß, J.-U., Tritscher, I., Höpfner, M., Pitts, M., Orr, A., and Riese, M.: A climatology of polar stratospheric cloud composition between 2002 and 2012 based on MIPAS/Envisat observations, Atmospheric Chemistry and Physics, 18, 5089–5113, https://doi.org/10.5194/acp-18-5089-2018, 2018.

https://doi.org/10.5194/egusphere-2026-128
Preprint. Discussion started: 23 February 2026


Steiner, M., Luo, B., Peter, T., Pitts, M. C., and Stenke, A.: Evaluation of polar stratospheric clouds in the global chemistry–climate model SOCOLv3.1 by comparison with CALIPSO spaceborne lidar measurements, Geoscientific Model Development, 14, 935–959, https://doi.org/10.5194/gmd-14-935-2021, 2021.

Stephens, G. L., Vane, D. G., Boain, R. J., Mace, G. G., Sassen, K., Wang, Z., Illingworth, A. J., O'connor, E. J., Rossow, W. B., Durden, S. L., Miller, S. D., Austin, R. T., Benedetti, A., and Mitrescu, C.: THE CLOUDSAT MISSION AND THE A-TRAIN: A New Dimension of Space-Based Observations of Clouds and Precipitation, Bulletin of the American Meteorological Society, 83, 1771–1790, https://doi.org/https://doi.org/10.1175/BAMS-83-12-1771, 2002.

Tesche, M., Achtert, P., and Pitts, M. C.: On the best locations for ground-based polar stratospheric cloud (PSC) observations, Atmospheric Chemistry and Physics, 21, 505–516, https://doi.org/10.5194/acp-21-505-2021, 2021.

Toon, O. B., Hamill, P., Turco, R. P., and Pinto, J.: Condensation of HNO3 and HCl in the winter polar stratospheres, Geophysical Research Letters, 13, 1284–1287, https://doi.org/https://doi.org/10.1029/GL013i012p01284, 1986.

Tritscher, I., Grooß, J.-U., Spang, R., Pitts, M. C., Poole, L. R., Müller, R., and Riese, M.: Lagrangian simulation of ice particles and resulting dehydration in the polar winter stratosphere, Atmospheric Chemistry and Physics, 19, 543–563, https://doi.org/10.5194/acp-19-543-2019, 2019.

Tritscher, I., Pitts, M. C., Poole, L. R., Alexander, S. P., Cairo, F., Chipperfield, M. P., Grooß, J.-U., Höpfner, M., Lambert, A., Luo, B., Molleker, S., Orr, A., Salawitch, R., Snels, M., Spang, R., Woiwode, W., and Peter, T.: Polar Stratospheric Clouds: Satellite Observations, Processes, and Role in Ozone Depletion, Reviews of Geophysics, 59, e2020RG000 702, https://doi.org/https://doi.org/10.1029/2020RG000702, 2021.

van den Broek, M. M. P., Williams, J. E., and Bregman, A.: Implementing growth and sedimentation of NAT particles in a global Eulerian model, Atmospheric Chemistry and Physics, 4, 1869–1883, https://doi.org/10.5194/acp-4-1869-2004, 2004.

Voigt, C., Larsen, N., Deshler, T., Kröger, C., Schreiner, J., Mauersberger, K., Luo, B., Adriani, A., Cairo, F., Di Donfrancesco, G., Ovarlez, J., Ovarlez, H., Dörnbrack, A., Knudsen, B., and Rosen, J.: In situ mountain-wave polar stratospheric cloud measurements: Implications for nitric acid trihydrate formation, Journal of Geophysical Research: Atmospheres, 108, https://doi.org/https://doi.org/10.1029/2001JD001185, 2003.

Voigt, C., Schlager, H., Luo, B. P., Dörnbrack, A., Roiger, A., Stock, P., Curtius, J., Vössing, H., Borrmann, S., Davies, S., Konopka, P., Schiller, C., Shur, G., and Peter, T.: Nitric Acid Trihydrate (NAT) formation at low NAT supersaturation in Polar Stratospheric Clouds (PSCs), Atmospheric Chemistry and Physics, 5, 1371–1380, https://doi.org/10.5194/acp-5-1371-2005, 2005.

Waters, J. W., Froidevaux, L., Harwood, R. S., Jarnot, R. F., Pickett, H. M., Read, W. G., Siegel, P. H., Cofield, R. E., Filipiak, M. J., Flower, D. A., Holden, J. R., Lau, G. K., Livesey, N. J., Manney, G. L., Pumphrey, H. C., Santee, M. L., Wu, D. L., Cuddy, D. T., Lay, R. R., Loo, M. S., Perun, V. S., Schwartz, M. J., Stek, P. C., Thurstans, R. P., Boyles, M. A., Chandra, K. M., Chavez, M. C., Chen, G.-S., Chudasama, B. V., Dodge, R., Fuller, R. A., Girard, M. A., Jiang, J. H., Jiang, Y., Knosp, B. W., LaBelle, R. C., Lam, J. C., Lee, K. A., Miller, D., Oswald, J. E., Patel, N. C., Pukala, D. M., Quintero, O., Scaff, D. M., Van Snyder, W., Tope, M. C., Wagner, P. A., and Walch, M. J.: The Earth observing system microwave limb sounder (EOS MLS) on the aura Satellite, IEEE Transactions on Geoscience and Remote Sensing, 44, 1075–1092, https://doi.org/10.1109/TGRS.2006.873771, 2006.

Weimer, M.: Towards Seamless Simulations of Polar Stratospheric Clouds and Ozone in the Polar Stratosphere with ICON-ART, Ph.D. thesis, https://doi.org/10.5445/IR/1000100338, 2019.

https://doi.org/10.5194/egusphere-2026-128
Preprint. Discussion started: 23 February 2026


Weimer, M., Buchmüller, J., Hoffmann, L., Kirner, O., Luo, B., Ruhnke, R., Steiner, M., Tritscher, I., and Braesicke, P.: Mountain-wave-induced polar stratospheric clouds and their representation in the global chemistry model ICON-ART, Atmospheric Chemistry and Physics, 21, https://doi.org/10.5194/acp-21-9515-2021, 2021.

Wilson, D. R. and Ballard, S. P.: A microphysically based precipitation scheme for the UK meteorological office unified model, Quarterly Journal of the Royal Meteorological Society, 125, 1607–1636, https://doi.org/https://doi.org/10.1002/qj.49712555707, 1999.

Zeng, G., Morgenstern, O., Williams, J. H. T., O'Connor, F. M., Griffiths, P. T., Keeble, J., Deushi, M., Horowitz, L. W., Naik, V., Emmons, L. K., Abraham, N. L., Archibald, A. T., Bauer, S. E., Hassler, B., Michou, M., Mills, M. J., Murray, L. T., Oshima, N., Sentman, L. T., Tilmes, S., Tsigaridis, K., and Young, P. J.: Attribution of Stratospheric and Tropospheric Ozone Changes Between 1850 and 2014 in CMIP6 Models, Journal of Geophysical Research: Atmospheres, 127, e2022JD036 452, https://doi.org/https://doi.org/10.1029/2022JD036452, 2022.

Zhu, Y., Toon, O. B., Lambert, A., Kinnison, D. E., Brakebusch, M., Bardeen, C. G., Mills, M. J., and English, J. M.: Development of a Polar Stratospheric Cloud Model within the Community Earth System Model using constraints on Type I PSCs from the 2010–2011 Arctic winter, Journal of Advances in Modeling Earth Systems, 7, 551–585, https://doi.org/https://doi.org/10.1002/2015MS000427, 2015.

Zhu, Y., Toon, O. B., Pitts, M. C., Lambert, A., Bardeen, C., and Kinnison, D. E.: Comparing simulated PSC optical properties with CALIPSO observations during the 2010 Antarctic winter, Journal of Geophysical Research: Atmospheres, 122, 1175–1202, https://doi.org/https://doi.org/10.1002/2016JD025191, 2017.